ANALYSIS OF RESOLUTION AND SENSITIVITY OF KELVIN PROBE FORCE MICROSCOPY

by

Bin Mao

Bachelor of Engineering in Automation, Beijing Jiaotong University, 2008

Submitted to the Graduate Faculty of

Swanson School of Engineering in partial fulfillment

of the requirements for the degree of

Master of Science in Electrical Engineering

University of Pittsburgh

2012

UNIVERSITY OF PITTSBURGH

SWANSON SCHOOL OF ENGINEERING

This thesis was presented

by

Bin Mao

It was defended on

April 3, 2012

and approved by

Hong Koo Kim, PhD, Bell of Pennsylvania/Bell Atlantic Professor, Department of Electrical and Computer Engineering

Zhi-Hong Mao, PhD, Associate Professor, Department of Electrical and Computer Engineering

Thesis Advisor: Guangyong Li, PhD, Assistant Professor, Department of Electrical and Computer Engineering

ANALYSIS OF RESOLUTION AND SENSITIVITY OF KELVIN PROBE FORCE MICROSCOPY

Bin Mao, M.S.

University of Pittsburgh, 2012

Kelvin probe force microscope (KPFM) has evolved into an effective tool to characterize electronic properties of materials and devices. However, there is lack of systematic analysis of its practical aspects such as resolution and sensitivity.

By analyzing the electrostatic model of the tip and sample, we can show that KPFM images are two-dimensional convolution of the actual surface potential distribution with a point spread function (PSF) derived from the tip geometry. Point spread function is a powerful tool, which can help us analyze the resolution. This thesis presents an analytical approach to find PSFs for probes with different geometric shapes in both amplitude-modulation and frequency-modulation KPFM.

Based on PSF, we can define the resolution of KPFM according to Raleigh criteria. With this definition, we analyze the resolution of KPFM image corresponding to different shapes and positions of tips. This method leads us to find an optimal shape of tip to obtain good resolution in KPFM. Also, the resolution of single-pass scan KPFM and dual-pass lift-up scan KPFM is compared. In addition, we investigate the sensitivity of KPFM under different operation modes with various scanning parameters. The findings in this research provide practical guidance for setting proper parameters in KPFM.

TABLE OF CONTENTS

1.0 INTRODUCTION 1

1.1 FUNDAMENTALS OF KPFM 1

1.1.1 Single-pass scan mode vs. dual-pass lift-up scan mode 2

1.1.2 Amplitude modulation KPFM vs. frequency modulation KPFM 3

1.2 POINT SPREAD FUNCTION AND ELECTROSTATIC FORCE MODELS .. 6

2.0 ELECTROSTATIC MODEL 8

2.1 THE POTENTIAL GENERATED BY THE TIP CHARGES 10

2.1.1 Determine the potential by using space charge density in free space 10

2.1.2 Determine the potential by using area charge density over a grounded plane 11

2.2 THE POTENTIAL CAUSED BY THE SAMPLE MODELED AS A DIPOLE LAYER 11

2.2.1 One dipole layer in free space 12

2.2.2 One dipole layer located over a grounded plane 13

2.3 THE BOUNDARY CONDTION 13

2.4 THE MINIMUM FORCE CONDITION FOR AM-KPFM 14

2.5 THE MINIMUM FORCE GRADIENT CONDITION FOR FM-KPFM 16

2.6 THE POINT SPREAD FUNCTION FOR A POINT 17

3.0 POINT SPREAD FUNCTIONS FOR DIFFERENT TIP PARAMETERS AND SCAN MODES 18

3.1 THE POINT SPREAD FUNCTIONS FOR DIFFERENT TIP SHAPES IN AM-KPFM MEASUREMENT 18

3.1.1 The point spread functions of a spherical shape tip with different tip parameters 20

3.1.2 The point spread functions of a conical shape tip with different tip parameters 22

3.1.3 The point spread function of a tip with both spherical part and conical part 24

3.1.4 The point spread functions of a tip consisted of spherical part, conical part with a carbon nanotube attached 25

3.2 THE POINT SPREAD FUNCTIONS FOR DIFFERENT TIP SHAPES IN FM-KPFM MEASUREMENT 26

4.0 RESOLUTION 31

4.1 RESOLUTION OF KPFM WITH AMPLITUDE MODULATION 32

4.2 RESOLUTION OF KPFM WITH FREQUENCY MODULATION 34

5.0 SENSITIVITY 37

5.1 ELECTROSTATIC FORCE FOR TIP WITH CARBON NANOTUBE ATTACHED 38

5.1.1 Spherical contribution 39

5.1.2 Conical contribution 39

5.1.3 Carbon nanotube contribution 40

5.2 SENSITIVITY OF AM-KPFM 41

5.3 SENSITIVITY OF FM-KPFM 42

5.4 SENSITIVITY COMPARASION 45

6.0 CONCLUSION 47

BIBLIOGRAPHY 49

LIST OF TABLES

Table 1. Comparison of resolution for the tip with spherical and conical part in AM-KPFM 32

Table 2. Comparison of resolution for the tip with carbon nanotube attached in AM-KPFM 34

Table 3. Comparison of resolution for the tip consisted of spherical and conical parts in FM-KPFM 35

Table 4. Comparison of resolution for FM-KPFM 36

LIST OF FIGURES

Figure 1. Electrical field distribution of a tip consisted of a hemispherical and a conical part. 7

Figure 2. Schematics of the tip-sample system used for electrostatic force modeling. 9

Figure 3. Hemisphere and flat sample surface 22

Figure 4. A tip consisted of hemispherical part, conical part with a carbon nanotube attached over flat sample surface 25

Figure 5. One-dimensional point spread functions of various tip shapes for different tip parameters in AM-KPFM measurement (a) One-dimensional PSFs of spherical tip for tip-sample distance, d of 1, 2, 5, 10, 20, 50 nm, R= 10 nm. (b) One-dimensional PSFs of spherical tip for tip apex radius, R of 1, 2, 5, 10, 20 nm, d=5 nm. (c) One-dimensional PSFs of tip consisted of spherical and conical parts for tip-sample distance, d of 1, 2, 5, 10, 20, 50 nm, R= 10 nm. (d) One-dimensional PSFs of tip consisted of spherical and conical parts for tip apex radius, R of 1, 2, 5, 10, 20 nm, d=5 nm. 28

Figure 6. One-dimensional point spread functions of various tip shapes for different tip parameters in FM-KPFM measurement (a) One-dimensional PSFs of spherical tip for tip-sample distance, d of 1, 2, 5, 10, 20, 50 nm, R= 10 nm. (b) One-dimensional PSFs of spherical tip for tip apex radius, R of 1, 2, 5, 10, 20 nm, d=5 nm. (c) One-dimensional PSFs of tip consisted of spherical and conical parts for tip-sample distance, d of 1, 2, 5, 10, 20, 50 nm, R= 10 nm. (d) One-dimensional PSFs of tip consisted of spherical and conical parts for tip apex radius, R of 1, 2, 5, 10, 20 nm, d=5 nm. 29

Figure 7. One-dimensional point spread functions of tip consisted of spherical part, and conical part with a carbon nanotube attached for different tip parameters (a) One-dimensional PSFs in AM-KPFM for the length of the carbon nanotube, l_{tw} of 0, 50, 100, 150, 200 nm, d = 5 nm, R= 15 nm, R_w = 1 nm. (b) One-dimensional PSFs in FM-KPFM for the length of the carbon nanotube, l_{tw} of 0, 50, 100, 150, 200 nm, d = 5 nm, R= 15 nm, R_w = 1 nm. 30

Figure 8. Resolution of AM-KPFM and FM-KPFM for different tip parameters (a) AM-KPFM Resolution vs. Tip-sample distance for tip apex radius, R=1 nm, 2 nm, 5 nm, 10 nm, 20 nm. (b) AM-KPFM Resolution vs. Tip apex radius for tip-sample distance, d=1 nm, 2 nm, 5 nm, 10 nm, 20 nm. (c) FM-KPFM Resolution vs. Tip-sample distance for tip apex radius, R=1 nm, 2 nm, 5 nm, 10 nm, 20 nm. (d) FM-KPFM Resolution vs. Tip apex radius for tip-sample distance, d=1 nm, 2 nm, 5 nm, 10 nm, 20 nm. 33

Figure 9. Sensitivity of tips with carbon nanotube attached in AM-KPFM, l_{tw} of 0, 50, 100, 150, 200 nm, d=1, 2, 5, 10 nm, R=15 nm, R_w=1nm (a) Sensitivity of AM-KPFM single scan vs. l_{tw} with different tip-sample distances, d. (b) Sensitivity of AM-KPFM single scan vs. tip-sample distances d with different l_{tw}. (c) Sensitivity of AM-KPFM dual-pass lift-up scan vs. l_{tw} with different tip-sample distances, d. (d) Sensitivity of AM-KPFM dual-pass lift-up scan vs. tip-sample distances d with different l_{tw} 44

Figure 10.Sensitivity of tips with carbon nanotube attached in FM-KPFM, l_{tw} of 0, 50, 100, 150, 200 nm, d=1, 2, 5, 10 nm, R=15 nm, R_w=1nm (a) Sensitivity vs. l_{tw} with different tip-sample distances, d. (b) Sensitivity vs. tip-sample distances d with different l_{tw} 45

1.0 INTRODUCTION

The atomic force microscopy (AFM) based Kelvin probe force microscopy has evolved into an effective tool to measure local surface potential distribution of metal/semiconductor surfaces and semiconductor devices. For example, KPFM has been used to investigate electrical properties of semiconductors [1-6] organic materials [7-9] and biomolecules [10-12] as well as devices such as photovoltaic cells [13-16] field effect transistors [17], and etc.

KPFM is an advanced mode of AFM. In KPFM measurements, both topographical image and contact surface potential image are obtained. The AFM tapping mode is usually utilized to obtain the topography of the sample. Tapping mode is an intermittent contact mode of AFM in which the cantilever is driven at, or close to its resonant frequency. As the tip-sample distance changes, the oscillation amplitude is also change from the reference amplitude. These changes are used as feedback signals to measure the topography of the sample surface. The details of the contact surface potential measurements will be explained in next section.

1.1 FUNDAMENTALS OF KPFM

A conductive AFM tip (coated with Pt/Ir or others) is usually used in KPFM measurements. We apply an AC voltage (V_{ac}) with angular frequency (ω_e) superimposed on a DC voltage (V_{dc}) on

the tip, such that $V = V_{dc} + V_{ac}\sin(\omega_e t)$. When this tip is brought close to the sample surface, electrostatic force is generated, which can be represented by the following equation: [12]

$$F_{el} = \frac{1}{2}\frac{\partial C}{\partial d}\left[\left(V_{dc} - V_{global}\right)^2 + \frac{1}{2}V_{ac}^2\right] + \frac{\partial C}{\partial d}\left(V_{dc} - V_{global}\right)V_{ac}\sin(\omega_e t) - \frac{1}{4}\frac{\partial C}{\partial d}V_{ac}^2\cos(2\times\omega_e t) \quad (1.1)$$

where, C is the capacitance between tip and sample surface, V_{global} is the surface potential distribution two-dimensional convoluted with a point spread function, d is tip-sample distance.

This electrostatic force consists of a static part and two contributions at ω_e and $2\omega_e$. The electrostatic force at the electrical driving frequency (ω_e) is:

$$F_{el}(\omega_e) = \frac{\partial C}{\partial d}\left(V_{dc} - V_{global}\right)V_{ac}\sin(\omega_e t) \quad (1.2)$$

The oscillation at the electrical driving frequency is majorly caused by the electrostatic force $F_{el}(\omega_e)$. The amplitude of the cantilever oscillation at the frequency (ω_e) can be detected and used as a feedback signal to nullify the electrostatic force $F_{el}(\omega_e)$ by adjusting the DC bias on the tip such that $V_{dc} = V_{global}$. The surface potential distribution can then be acquired from the DC bias $V_{global} = V_{dc}$.

1.1.1 Single-pass scan mode vs. dual-pass lift-up scan mode

Now, KPFM has been implemented into two basic scanning modes, single-pass scan mode and dual-pass lift-up scan mode. Dual-pass lift-up scan mode acquires the topography using AFM's tapping mode in the first pass. And then the conductive tip is lifted up by a small distance (10~20nm) above the sample surface and applied an AC voltage with the same frequency as the tip's resonant frequency, superimposed on a DC voltage. By following the exact surface

topography acquired in the first pass, the surface potential information can be obtained in the second pass. The advantage of this mode is that coupling of topography and surface potential can be minimized since these two measurements are preformed separately. Furthermore, the electrical drive frequency of dual-pass lift-up scan is set at the cantilever's mechanical resonant frequency, which will lead to higher sensitivity. Because the resolution of KPFM highly depends on the tip-sample distance, the dual-pass lift-up scan mode, which lifts the tip up and increases the tip-sample distance, leads to low spatial resolution.

Single-pass scan mode uses one feedback loop to nullify the electrostatic force $F_{el}(\omega_e)$ induced oscillation amplitude to acquire the measured surface potential and uses another feedback loop to lock in the mechanical drive frequency (ω_m) to acquire topographical information. Both topography and surface potential image can be obtained at the same time in single-pass scan KPFM. Single-pass scan mode performs much better than dual-pass lift-up scan mode in terms of resolution and accuracy. However, this mode requires different electrical drive frequency from the resonant frequency of the tip, which will affect the sensitivity of KPFM measurement, and may cause crosstalk.

1.1.2 Amplitude modulation KPFM vs. frequency modulation KPFM

Amplitude modulation KPFM acquires surface potential distribution images by nullifying the oscillation amplitude at ω_e , while frequency modulation KPFM minimizes the oscillation amplitude at $\omega_0 + \omega_e$ where ω_0 is the resonant frequency of the cantilever and tip system.

The oscillation pattern at these two lock-in frequencies is one of the major difference between these two modes, and of great importance for studying the sensitivity.

For a cantilever with resonant frequency ω_0 and quality factor Q, the oscillation amplitude A_e at electrical drive frequency ω_e in AM-KPFM measurement, under a driving force, $F_{el}(\omega_e)$, can be calculated from the following equation:

$$A_e = \frac{F_d(\omega_e)}{k} \sqrt{\frac{1}{(1-\frac{\omega_e^2}{\omega_0^2})^2 + \frac{1}{Q^2}\frac{\omega_e^2}{\omega_0^2}}} \quad (1.3)$$

where k is the spring constant of the cantilever and F_d is the force amplitude at ω_e. If we plug **Equation (1.2)** into **Equation (1.3)**, we can get

$$A_e = \frac{\partial C/\partial d \left(V_{dc} - V_{global}\right) V_{ac}}{k} \sqrt{\frac{1}{(1-\frac{\omega_e^2}{\omega_0^2})^2 + \frac{1}{Q^2}\frac{\omega_e^2}{\omega_0^2}}} \quad (1.4)$$

In AM-KPFM, a lock-in amplifier locks in the electrical drive frequency to detect A_e. A_e is then nullified by adjusting the DC voltage such that $V_{dc} = V_{global}$. This is equivalent to nullify electrostatic force at the electrical drive frequency, ω_e. In single-pass scan AM-KPFM, the mechanical drive is set at, or close to, the resonant frequency of the cantilever while the electrical drive is set at a lower frequency than the resonant frequency. In dual-pass lift-up scan AM-KPFM, the electrical drive and the mechanical drive can be both set at the resonant frequency of the cantilever.

AM-KPFM minimizes the electrostatic force. On the contrary, FM-KPFM detects the force gradient, which has already been proved that its effect is much more confined to the tip apex than the force [18]. In FM-KPFM measurements, with the presence of small force gradient $\partial F/\partial d$, the phase of the oscillation at the drive frequency ω_0 shifts

$\Delta\varphi = -Q(\partial F/\partial d)/k$. Noting **Equation (1.1)**, the oscillation of cantilever at resonant frequency becomes

$$A(t) = A_0 \sin\left\{\omega_m t - \frac{Q}{2k}\frac{\partial^2 C}{\partial d^2}\left[\left(\left(V_{dc} - V_{global}\right)^2 + \frac{1}{2}V_{ac}^2\right) + 2\left(V_{dc} - V_{global}\right)V_{ac}\cos(\omega_e t) - \frac{1}{2}V_{ac}^2\cos(2\omega_e t)\right]\right\} \quad (1.5)$$

When the phase shift is small, **Equation (1.5)** can be written as the following form

$$A(t) = A_0 \sin(\omega_m t - \phi) + 2A_{m\pm e}\sin(\omega_e t)\cos(\omega_m t - \phi) + 2A_{m\pm 2e}\cos(2\omega_e t)\cos(\omega_m t - \phi) \quad (1.6)$$

where

$$\phi = \frac{Q}{2k}\frac{\partial^2 C}{\partial d^2}\left(\left(V_{dc} - V_{global}\right)^2 + \frac{1}{2}V_{ac}^2\right),$$

$$A_{m\pm e} = -A_0\frac{Q}{2k}\frac{\partial^2 C}{\partial d^2}\left(V_{dc} - V_{global}\right)V_{ac},$$

$$A_{m\pm 2e} = -A_0\frac{Q}{8k}\frac{\partial^2 C}{\partial d^2}V_{ac}^2$$

This $A_{m\pm e}$ represents the oscillation amplitude at the sidebands $\omega_m \pm \omega_e$. In FM-KPFM, the oscillation amplitude at the sidebands $\omega_m \pm \omega_e$ is detected through a lock-in amplifier. The control loop nullifies the amplitude at the sidebands $\omega_m \pm \omega_e$ by adjusting the DC voltage such that $V_{dc} = V_{global}$. In ambient FM-KPFM, the mechanical drive is often set at the resonant frequency of the cantilever while the electrical drive is set at a lower frequency than the resonant frequency.

1.2 POINT SPREAD FUNCTION AND ELECTROSTATIC FORCE MODELS

Because Columbic interaction (the electrostatic force) is a long-range force, the surfaces on tip apex, the tip cone, and the cantilever all have interaction with the sample surface. When the surface potential is not constant, the KPFM-measured potential is a weighted result from a much larger effective area than the tip apex. The surface contact potential difference, V_{global}, in **Equation (1.1)** becomes a 2D convolution of a point spread function (PSF) and surface potentials over a large effective area such that

$$V_{global} = h(x - x_t, y - y_t) * \Phi^S(x, y) \qquad (1.6)$$

where (x_t, y_t) represents the tip location, $h(x - x_t, y - y_t)$ is a PSF, $\Phi^S(x, y)$ is the surface potential difference at (x,y). Basically there are two different models presented and analyzed by several authors to derive the PSFs.

Jacob et al. derived the PSF based on a capacitance model that formulates a set of ideal conductors with mutual capacitances between a semiconductor specimen and the tip. [19]. But this method suffers from a few drawbacks. In this model, we can calculate the capacitances either by finding the ratio of the charge on the tip and the potential difference, or by using the tip geometry. For the first approach, the charge on tip is difficult to find. For the latter one, the whole idea is based on the assumption that the electric field has same magnitude along the field lines. In **Figure 1**, those arrows denote the direction and the magnitude of the electric field lines. From **Figure 1**, we can see that the magnitude along the field lines varies a lot. Following this model will give us inaccurate electrostatic force and point spread function.

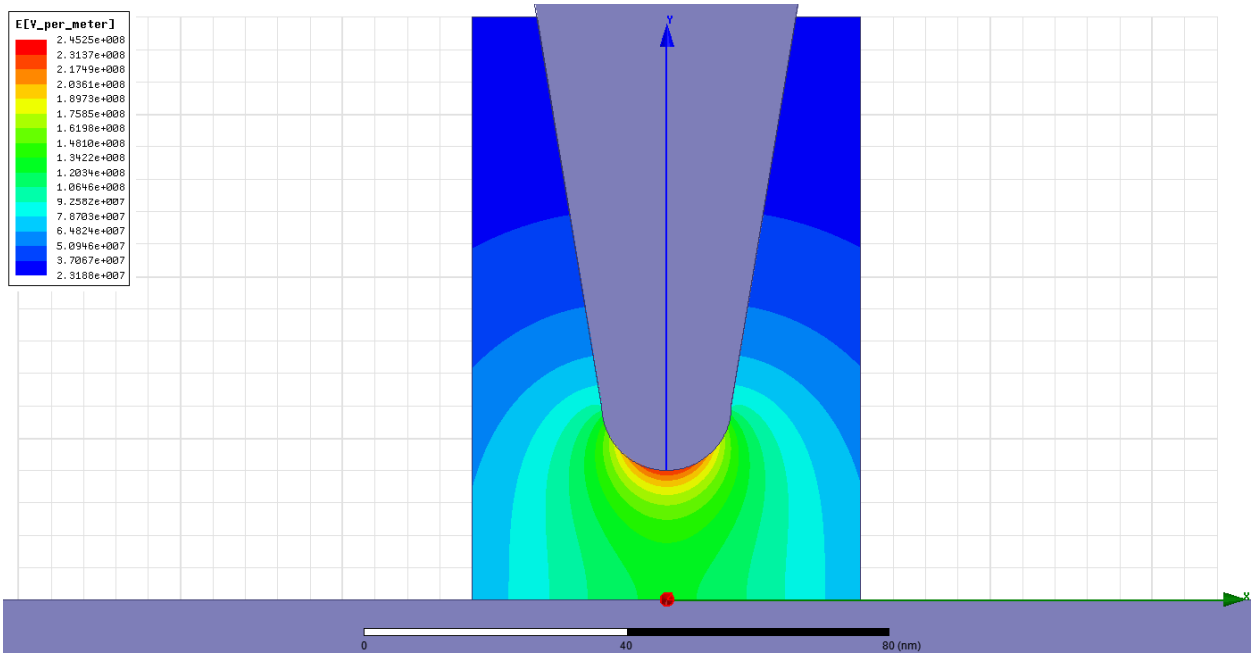

Figure 1. Electrical field distribution of a tip consisted of a hemispherical and a conical part.

Strassburg et al. introduced another model to evaluate the electrostatic force between conductive tip and semiconductor specimen by using the boundary element method [20]. Using this method, the electrostatic force is determined only by the charge density on the tip surface. So that we can calculate electric field near the tip surface and acquire more accurate results. Since the charge density is only an intermediate variable that we can cancel later on, there is no need to find the exact value of the charge density. So this method overcomes the problems in the ideal capacitance model.

2.0 ELECTROSTATIC MODEL

A conductive tip with a length l, half aperture angle θ, spherical apex radius R and a surface S^t, is located at a height d above the sample with planar surface placed on a grounded plane at the z = 0 plane (**Figure 2**). We use a notation r to represent the vector point to the tip surface S^t in the (x, y, z) space.

In AM-KPFM measurements, the tip potential V_{dc} is applied to minimize z-direction force. Hudlet et al. prove that minimizing z-direction force is equivalent to nullify the modulated force at the electrical drive frequency [20]. In FM-KPFM measurements, the force gradient was used as interaction signal. Minimizing z-direction force gradient is also equivalent to nullify the modulated force at the electrical drive frequency. We will have a detailed discussion about that in **Section 2.4 and 2.5**.

The surface potential is modeled by a dipole layer located on the top of a grounded plane at z = 0. The potential of any point in the upper half-space is consisted of the potential generated by the charge dwelling on the tip surface $\Phi^t(r)$ and the potential generated by the dipole layer $\Phi^d(r)$. $\Phi^t(r)$ and $\Phi^d(r)$ will be determined separately.

Charge density is used as an intermediate variable. By imposing boundary condition along with either minimum force or minimum force gradient condition, we can cancel the intermediate variable and find the relation between surface potential $\Phi^S(x,y)$ and the measured V_{dc}.

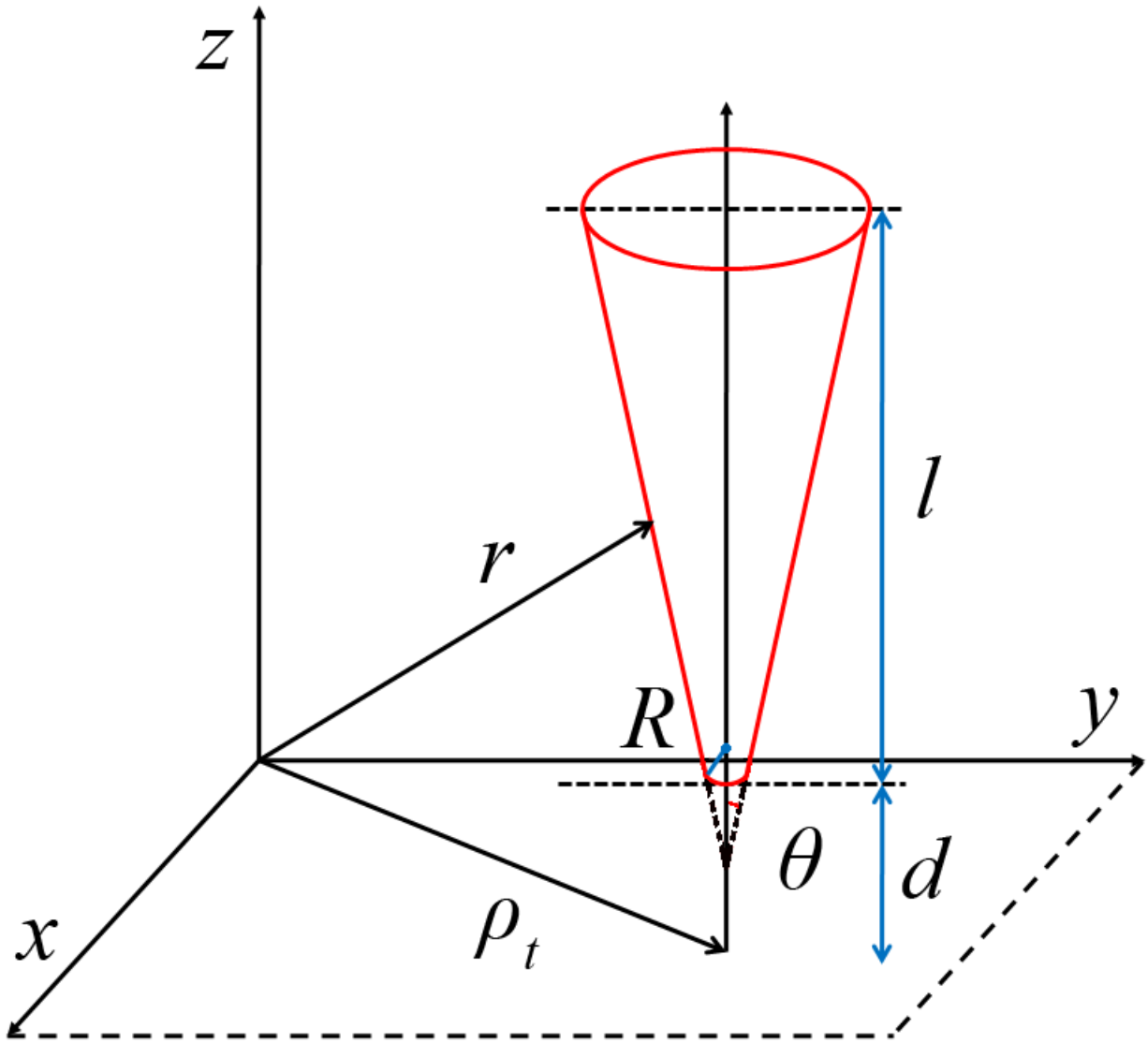

Figure 2. Schematics of the tip-sample system used for electrostatic force modeling.

2.1 THE POTENTIAL GENERATED BY THE TIP CHARGES

In this section, the potential generated by the tip charges $\Phi^t(r)$ was determined by using the method of images. Based on the tip geometry, we can find the relation between tip charge density and $\Phi^t(r)$.

2.1.1 Determine the potential by using space charge density in free space

Based on Coulomb's law, the electric field at position r due to a system of point charges q_i, located at r_i, i=1, 2, …, n, can be represented by the following equation:

$$E(r) = \frac{1}{4\pi\varepsilon_0}\sum_{i=1}^{n} q_i \frac{r - r_i}{|r - r_i|^3} \quad (2.1)$$

The sum can be replaced by an integral

$$E(r) = \frac{1}{4\pi\varepsilon_0}\int_V \rho(r')\frac{r - r'}{|r - r'|^3}dr' = -\frac{1}{4\pi\varepsilon_0}\nabla\int_V \frac{\rho(r')}{|r - r'|}dr' \quad (2.2)$$

where $\rho(r')$ is the space charge density at r'. Based on the well known equation $E = -\nabla\Phi$, where Φ is the potential, we have

$$\Phi(r) = \frac{1}{4\pi\varepsilon_0}\int_V \frac{\rho(r')}{|r - r'|}dr' \quad (2.3)$$

where $\Phi(r)$ is the potential generated by the charges resided in space V.

2.1.2 Determine the potential by using area charge density over a grounded plane

The charge of the conductive tip dwell on its surface, so the potential caused by the charges in free space can be expressed as:

$$\Phi(r) = \frac{1}{4\pi\varepsilon_0}\int_{S^t}\frac{\sigma(r')}{|r-r'|}ds \qquad (2.4)$$

where $\sigma(r')$ is the area charge density at r'.

Because we place the sample on a grounded plane, the image method should be utilized here by placing the negative charge tip on the other side of the sample to make the potential on the plane equal 0. Thus we have the potential caused by the tip charges,

$$\Phi^t(r) = \frac{1}{4\pi\varepsilon_0}\int_{S^t}\frac{\sigma(r')}{|r-r'|}ds' - \frac{1}{4\pi\varepsilon_0}\int_{S^t}\frac{\sigma(r'')}{|r-r''|}ds' \qquad (2.5)$$

where $r'' = (x', y', -z')$ is the image point of $r' = (x', y', z')$.

2.2 THE POTENTIAL CAUSED BY THE SAMPLE MODELED AS A DIPOLE LAYER

In this section, we want to find the relation between the potential caused by the dipole layer $\Phi^d(r)$ and the actual sample surface potential $\Phi^S(x, y)$.

2.2.1 One dipole layer in free space

We model the sample surface as a dipole layer placed on a grounded plane. To find the potential generated by a dipole layer, we should first consider a single dipole and then superpose a surface density of them [21].

With $\hat{n}$, the unit normal to the sample surface S, the potential due to the two close surfaces of a dipole is

$$\Phi(\mathrm{r}) = \frac{1}{4\pi\varepsilon_0}\int_S \frac{\sigma^S(\mathrm{r}')}{|\mathrm{r}-\mathrm{r}'|}\mathrm{ds}' - \frac{1}{4\pi\varepsilon_0}\int_S \frac{\sigma^S(\mathrm{r}')}{|\mathrm{r}-\mathrm{r}'+\hat{\mathrm{n}}\mathrm{d}_{\mathrm{dipole}}|}\mathrm{ds}' \quad (2.6)$$

where $\mathrm{d}_{\mathrm{dipole}}$ is the small distance between the two surface of a dipole, r' is a point on the small surface s'.

Since d is very small, we can expand $\frac{1}{|\mathrm{r}-\mathrm{r}'+\hat{\mathrm{n}}\mathrm{d}_{\mathrm{dipole}}|}$ with a Taylor series expansion in three dimensions:

$$\frac{1}{4\pi\varepsilon_0}\int_S \frac{\sigma^S(\mathrm{r}')}{|\mathrm{r}-\mathrm{r}'+\hat{\mathrm{n}}\mathrm{d}_{\mathrm{dipole}}|}\mathrm{ds}' = \frac{1}{4\pi\varepsilon_0}\int_S \frac{\sigma^S(\mathrm{r}')}{|\mathrm{r}-\mathrm{r}'|}\mathrm{ds}' - \frac{1}{4\pi\varepsilon_0}\int_S \hat{\mathrm{n}}\cdot\mathrm{d}_{\mathrm{dipole}}\cdot\nabla'\frac{\sigma^S(\mathrm{r}')}{|\mathrm{r}-\mathrm{r}'|}\mathrm{ds}' \quad (2.7)$$

Plug **Equation (2.7)** into **Equation (2.6)**, we have

$$\Phi(\mathrm{r}) = \frac{1}{4\pi\varepsilon_0}\int_S \hat{\mathrm{n}}\cdot\mathrm{d}_{\mathrm{dipole}}\cdot\nabla'\frac{\sigma^S(\mathrm{r}')}{|\mathrm{r}-\mathrm{r}'|}\mathrm{ds}' = \frac{1}{4\pi\varepsilon_0}\int_S \sigma^S(\mathrm{r}')\cdot\mathrm{d}_{\mathrm{dipole}}\cdot\frac{\partial\frac{1}{|\mathrm{r}-\mathrm{r}'|}}{\partial\mathrm{z}'}\bigg|_{\mathrm{z}'=0}\mathrm{ds}' \quad (2.8)$$

According to Gauss' Law, we have $\mathrm{E}\cdot\hat{\mathrm{n}}\cdot\mathrm{d}_{\mathrm{dipole}} = \frac{\sigma\cdot\mathrm{d}_{\mathrm{dipole}}}{\varepsilon_0} = \Phi^S(\mathrm{r})$, where Φ^S represents the surface potential, we can find the relation between the potential generated by one dipole layer and the surface potential of the dipole layer by plugging this equation into **Equation (2.8)**,

$$\Phi(r) = \frac{1}{4\pi}\int_S \left.\frac{\partial \frac{1}{|r-r'|}}{\partial z'}\right|_{z'=0} \Phi^S(s')ds' \quad (2.9)$$

2.2.2 One dipole layer located over a grounded plane

Because d_{dipole} is very small, when we use image method by placing another dipole layer on the other side of the grounded plane to make the potential on the plane equal 0, we can neglect this small distance d_{dipole}. The potential caused by these two dipole layers is given by

$$\Phi^d(r) = 2\Phi(r) = \frac{1}{2\pi}\int_S \left.\frac{\partial \frac{1}{|r-r'|}}{\partial z'}\right|_{z'=0} \Phi^S(s')ds' \quad (2.10)$$

2.3 THE BOUNDARY CONDTION

In this section, we will connect the measured potential V(r) with the actual surface potential by imposing the boundary condition. You will see that the measured potential V(r) is also a function of charge density, but this charge density will be canceled later on.

The total potential at any point in the upper half-space, z>0, is given by the superposition

$$\Phi(r) = \Phi^t(r) + \Phi^d(r) \quad (2.11)$$

where $\Phi^t(r)$ is the potential produced by the charges residing on the tip, and $\Phi^d(r)$ is the potential generated by the dipole layer.

Since the tip surface is conductive, we assume that the tip surface is equipotential. So we can impose the boundary condition $\Phi(r)\Big|_{r \in S^t} = V(r)$ where $\Phi(r)\Big|_{r \in S^t}$ is the potential on the tip surface and V(r) is the measure potential when r=(x, y, z).

Employing **Equation (2.11)**, we obtain an integral equation for the tip surface charge density

$$V(r) = \frac{1}{4\pi\varepsilon_0}\int_{S^t}\frac{\sigma(r')}{|r-r'|}ds' - \frac{1}{4\pi\varepsilon_0}\int_{S^t}\frac{\sigma(r'')}{|r-r''|}ds' + \frac{1}{2\pi}\int_S \frac{\partial\frac{1}{|r-r'|}}{\partial z'}\Big|_{z'=0}\Phi^S(s')ds',\ r \in S^t \qquad (2.12)$$

where $r'' = (x', y', -z')$ is the image point of $r' = (x', y', z')$.

2.4 THE MINIMUM FORCE CONDITION FOR AM-KPFM

For amplitude-modulation KPFM, minimizing the vertical electrostatic force is equivalent to nullifying the oscillation amplitude at electrical drive frequency. AM-KPFM works by applying an ac voltage with frequency ω_e and amplitude V_{ac}, superimposed on a dc voltage V between tip and sample. Under this configuration, the electrostatic force F_{el} is given by **Equation (1.1)** as follows

$$F_{el} = \frac{1}{2}\frac{\partial C}{\partial d}\left[\left(V_{dc} - V_{global}\right)^2 + \frac{1}{2}V_{ac}^2\right] + \frac{\partial C}{\partial d}\left(V_{dc} - V_{global}\right)V_{ac}\sin(\omega_e t) - \frac{1}{4}\frac{\partial C}{\partial d}V_{ac}^2\cos(2\times\omega_e t)$$

where C is the capacitance of the tip-sample system, V_{global} is the 2D convolution of point spread function and surface potential, d is tip-sample distance.

This electrostatic force consists of a static part and two contributions at ω_e and $2\omega_e$. We can see from **Equation (1.1)** that the amplitude at ω_e is nullified as the static part minimized.

Consider a small area on tip surface with area charge density $\sigma(r)$ and the unit normal $\hat{n}$, the electrical field in this area can be expressed as $E = \frac{\sigma(r)}{\varepsilon_0}\hat{n}$. The electrical field this charged area generated should be subtracted when we calculate the vertical force. Based on Gauss's law, half of E in $\hat{n}$ direction should be subtracted, so $E_{out} = \frac{\sigma(r)}{2\varepsilon_0}\hat{n}$, $dF = \frac{\sigma^2(r)}{2\varepsilon_0}\hat{n}ds$, where E_{out} is the electrical field generated by other sources outside this charged area.

The electrostatic force F can be obtained by an integral

$$F = \int_{S^t} \frac{\sigma^2(r)}{2\varepsilon_0}\hat{n}ds \qquad (2.13)$$

The z component of the force can be expressed as

$$F_z = \int_{S^t} \frac{\sigma^2(r)}{2\varepsilon_0}\hat{n}\cdot\hat{z}ds \qquad (2.14)$$

The minimum force condition $\frac{\partial F_z}{\partial V} = 0$ can be expressed via **Equation (19)** as

$$\frac{\partial F_z}{\partial V} = \frac{\partial \int_{S^t} \frac{\sigma^2(r)}{2\varepsilon_0}\hat{n}\cdot\hat{z}ds}{\partial V} = 0 \qquad (2.15)$$

2.5 THE MINIMUM FORCE GRADIENT CONDITION FOR FM-KPFM

For frequency-modulation KPFM, a better measurement of surface potential can be achieved by using the force gradient as interaction signal [22]. Take derivative of **Equation (1.1)**, the force gradient is given by

$$F_{el}^{'} = \frac{1}{2}\frac{\partial^2 C}{\partial d^2}\left[\left(V_{dc} - V_{global}\right)^2 + \frac{1}{2}V_{ac}^2\right] + \frac{\partial^2 C}{\partial d^2}\left(V_{dc} - V_{global}\right)V_{ac}\sin(\omega_e t) - \frac{1}{4}\frac{\partial^2 C}{\partial d^2}V_{ac}^2\cos(2\times\omega_e t) \quad (2.16)$$

In order to let $V_{dc} = V_{global}$, the static part of the force gradient should be minimized with respect to tip potential V. Take derivative of **Equation (2.15)** with respect to tip-sample distance d will give

$$\frac{\partial \mathrm{F_z}}{\partial \mathrm{d}} = \frac{\partial \int_{S^t} \frac{\sigma^2(\mathrm{r})}{2\varepsilon_0}\hat{\mathrm{n}}\cdot\hat{\mathrm{z}}\mathrm{ds}}{\partial \mathrm{d}} \quad (2.17)$$

The minimum force gradient condition $\frac{\partial^2 \mathrm{F_z}}{\partial \mathrm{d}\partial \mathrm{V}} = 0$ can be expressed via **Equation (2.17)** as

$$\frac{\partial^2 \mathrm{F_z}}{\partial \mathrm{d}\partial \mathrm{V}} = \frac{\partial^2 \int_{S^t} \frac{\sigma^2(\mathrm{r})}{2\varepsilon_0}\hat{\mathrm{n}}\cdot\hat{\mathrm{z}}\mathrm{ds}}{\partial \mathrm{d}\partial \mathrm{V}} = 0 \quad (2.18)$$

2.6 THE POINT SPREAD FUNCTION FOR A POINT

If we only consider the presence of the dipole layer, the dipole layer's contribution to the potential on the observation point can be expressed as a convolution by employing **Equation (2.10)**,

$$\Phi^{d}(r) = h_{d}(x,y) * \Phi^{S}(x,y) = \frac{1}{2\pi} \frac{\partial \frac{1}{|r - z'|}}{\partial z'}\bigg|_{z'=0} * \Phi^{S}(x,y) \qquad (2.19)$$

So the point spread function for a point (x_t, y_t, z_t) is

$$h_d(x,y) = \frac{1}{2\pi} \frac{\partial \frac{1}{\sqrt{x^2 + y^2 + (z_t - z')^2}}}{\partial z'}\bigg|_{z'=0} = \frac{z_t}{2\pi}(x^2 + y^2 + z_t^2)^{-\frac{3}{2}} \qquad (2.20)$$

3.0 POINT SPREAD FUNCTIONS FOR DIFFERENT TIP PARAMETERS AND SCAN MODES

In this section, we will find the point spread functions for AM-KPFM and FM-KPFM corresponding to different tip parameters. The integral **Equation (2.12)** is difficult to solve because of the unknown charge density on the tip surface. So we will introduce a finite elements analysis to cancel this charge density.

3.1 THE POINT SPREAD FUNCTIONS FOR DIFFERENT TIP SHAPES IN AM-KPFM MEASUREMENT

For AM-KPFM, Strassburg et al. [20] proposed a method to split the tip surface into a set of elements $\{S_i^t\}_{i=1}^N$ such that $S^t = \bigcup_{i=1}^N S_i^t$. We assume each small area S_i^t has the same charge density. **Equation (2.12)** can then be written as

$$[A]\vec{\sigma} = V\vec{1} - \vec{\Phi}^d \qquad (3.1)$$

where [A] is an N by N matrix whose ijth element is given by

$$A_{ij} = \frac{1}{4\pi\varepsilon_0}\int_{S_j^t}\frac{1}{|r_i - r'|}ds' - \frac{1}{4\pi\varepsilon_0}\int_{S_j^t}\frac{1}{|r_i - r''|}ds' \qquad (3.2)$$

A_{ij} represents the contribution of charge density in S_j^t to the potential in S_i^t. In **Equation (3.1)**, $\vec{\sigma}$, $\vec{1}$ and $\vec{\Phi}^d$ are N vectors whose ith elements are $\vec{\sigma}_i$, 1, and $\vec{\Phi}^d(r_i)$, respectively. The charge density can be solved as

$$\vec{\sigma} = [A]^{-1}(V\vec{1} - \vec{\Phi}^d) \qquad (3.3)$$

We need to plug **Equation (3.3)** into minimum force condition to solve for V and cancel this $\vec{\sigma}$. In discrete form, electrostatic force in z direction, **Equation (2.14)**, can be expressed as

$$F_z = \vec{\sigma}^t [B] \vec{\sigma} \qquad (3.4)$$

where [B] is an N by N diagonal matrix whose ith diagonal element is given by

$$B_{ii} = \int_{S_i^t} \frac{1}{2\varepsilon_0} \hat{n} \cdot \hat{z} ds \qquad (3.5)$$

where $\hat{z}$ denotes a unit vector in the z direction. The minimum force condition $\frac{\partial F_z}{\partial V} = 0$ can be expressed via **Equation (3.4)**

$$\left(\frac{\partial \vec{\sigma}}{\partial V}\right)^t [B] \vec{\sigma} = 0 \qquad (3.6)$$

We plug **Equation (3.3)** into **Equation (3.6)** and obtain the relation between the measured tip potential and the potential produced by the dipole layer:

$$V(r) = \left\{ \left([A]^{-1}\vec{1}\right)^t [B][A]^{-1}\vec{1} \right\}^{-1} \left([A]^{-1}\vec{1}\right)^t [B][A]^{-1}\vec{\Phi}^d(r) \qquad (3.7)$$

Since $\vec{\Phi}^d(r)$ can be represented by a two-dimensional convolution of the surface potential and a mask in **Equation (2.19)**, we find that the measured tip potential can be expressed as

$$V(x,y) = h_{AM}(x,y) * \Phi^S(x,y) \qquad (3.8)$$

with the continuous point spread function,

$$h_{AM}(x,y) = \left\{\left([A]^{-1}\vec{1}\right)^t [B][A]^{-1}\vec{1}\right\}^{-1}\left([A]^{-1}\vec{1}\right)^t [B][A]^{-1}\vec{h}_d \qquad (3.9)$$

3.1.1 The point spread functions of a spherical shape tip with different tip parameters

For a spherical tip surface (**Figure 3**) with tip-sample distance d and radius R, we can split the cone into n segments in z-direction, and then we equally split one segment into m pieces in 360 degree to form a small area S_i^t. We need to carefully choose the value of m to avoid singularity of matrix [A]. We first determine [A] matrix based on **Equation (3.2)**.

$$A_{ij} = \frac{1}{4\pi\varepsilon_0}\int_{S_j^t}\frac{1}{|r_i - r'|}ds' - \frac{1}{4\pi\varepsilon_0}\int_{S_j^t}\frac{1}{|r_i - r''|}ds'$$

where $ds' = R^2 \sin\beta d\beta d\varphi$.

The first term of A_{ij} can be written as:

$$A1_{ij} = \frac{1}{4\pi\varepsilon_0}\int_{\varphi_{j-1}}^{\varphi_j}\int_{\arcsin(\lfloor j/m \rfloor/n)}^{\arcsin(\lceil j/m \rceil/n)} \frac{R^2\sin\beta}{\sqrt{R^2-(d+R-z_i)^2+\sin^2\beta R^2-2\cos\varphi\sin\beta R\sqrt{R^2-(d+R-z_i)^2}+(d+R-z_i-\cos\beta R)^2}} d\beta d\varphi \qquad (3.10)$$

The second part of Aij can be written as

$$A2_{ij} = \frac{1}{4\pi\varepsilon_0}\int_{\varphi_{j-1}}^{\varphi_j}\int_{\arcsin(\lfloor j/m \rfloor/n)}^{\arcsin(\lceil j/m \rceil/n)} \frac{R^2\sin\beta}{\sqrt{R^2-(d+R-z_i)^2+\sin^2\beta R^2-2\cos\varphi\sin\beta R\sqrt{R^2-(d+R-z_i)^2}+(d+R+z_i-\cos\beta R)^2}} d\beta d\varphi$$

(3.11)

where $z_i = d + R - \sqrt{R^2 - x_i^2 - y_i^2}, (x_i, y_i, z_i) \in S_i^t$.

We then can find the explicit expression of [A], whose ijth element is $A_{ij} = A1_{ij} - A2_{ij}$

We can determine matrix [B] from **Equation (3.5)**

$$B_{ii} = \int_{S_i^t}\frac{1}{2\varepsilon_0}\hat{n}\cdot\hat{z}ds$$

where $\hat{z}ds = (d + R - z_i)dzd\varphi$.

So B_{ii} can be written as

$$B_{ii} = \frac{1}{2\varepsilon_0}\int_{\varphi_{i-1}}^{\varphi_i}\int_{d+R-\sqrt{R^2-\left(\left\lfloor\frac{i}{m}\right\rfloor\right)^2 R^2/n^2}}^{d+R-\sqrt{R^2-\left(\left\lfloor\frac{i}{m}\right\rfloor\right)^2 R^2/n^2}}(d + R - z_i)dzd\varphi \qquad (3.12)$$

where $z_i = d + R - \sqrt{R^2 - x_i^2 - y_i^2}, (x_i, y_i, z_i) \in S_i^t$

With [A] and [B], we can determine the continuous point spread function for the conical part of the tip from **Equation (3.9)**.

$$h_{AM}(x, y) = \left\{\left([A]^{-1}\vec{1}\right)^t [B][A]^{-1}\vec{1}\right\}^{-1}\left([A]^{-1}\vec{1}\right)^t [B][A]^{-1}\vec{h}_d$$

where $\vec{h}_d$ is an N vector whose ith element is the ith segment's point spread function for a point $(x_i, y_i, z_i) \in S_i^t$ on the ith segment of tip surface. It can be represented by the following equation:

$$h_{d,i}(x, y) = \frac{z_i}{2\pi}\left[(x - x_i)^2 + (y - y_i)^2 + z_i^2\right]^{-\frac{3}{2}} \qquad (3.13)$$

where $z_i = d + R - \sqrt{R^2 - x_i^2 - y_i^2}, (x_i, y_i, z_i) \in S_i^t$.

We choose typical KPFM tip parameters: length $l = 10\mu m$, half-aperture angle $\theta = 22.5^\circ$. One-dimensional point spread functions calculated for various tip parameters are shown in **Figure 5 (a), (b)**.

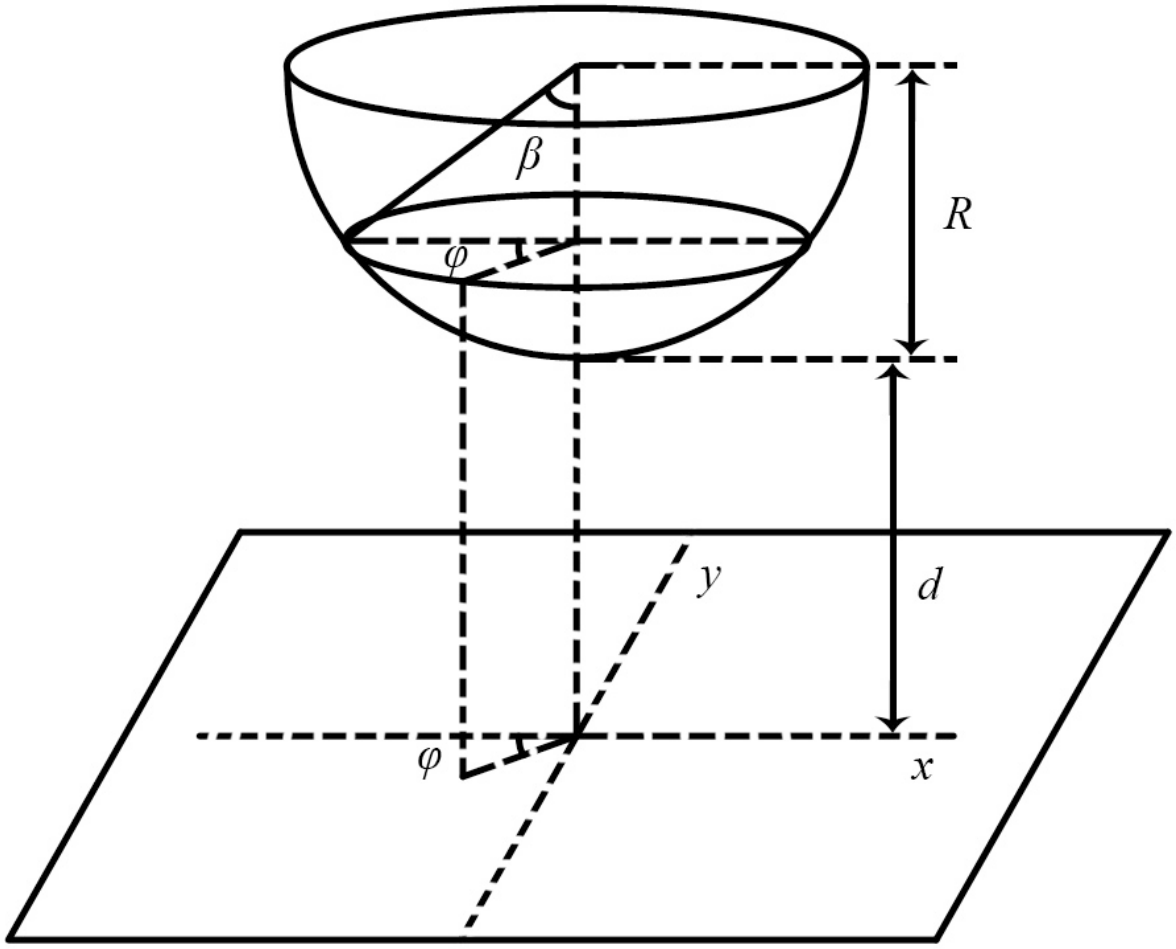

Figure 3. Hemisphere and flat sample surface

3.1.2 The point spread functions of a conical shape tip with different tip parameters

For a conical tip surface (similar to **Figure 2**) with tip-sample distance d, and length l, we can split the cone into n segments in z-direction, and then we equally split one segment into m pieces in 360 degree to form a small area S_i^t. The number of m should be chosen carefully to avoid singularity of matrix [A]. We first determine [A] matrix based on **Equation (3.2)**.

$$A_{ij} = \frac{1}{4\pi\varepsilon_0}\int_{S_j^t}\frac{1}{|r_i - r'|}ds' - \frac{1}{4\pi\varepsilon_0}\int_{S_j^t}\frac{1}{|r_i - r''|}ds'$$

where $\mathrm{ds}' = \dfrac{(z'-z_f)\tan\theta}{\cos\theta}\mathrm{dz}'\,\mathrm{d}\varphi$, $z_f = d + R - R/\sin\theta$ is the apex of the cone.

The first part of Aij can be written as

$$A1_{ij} = \frac{1}{4\pi\varepsilon_0}\int_{\varphi_{j-1}}^{\varphi_j}\int_{\frac{(l-R)(j-1)}{n}+d+R}^{\frac{(l-R)j}{n}+d+R}\frac{(z'-z_f)\tan\theta/\cos\theta}{\sqrt{(z_i-z')^2+(z_i-z_f)^2\tan^2\theta+(z'-z_f)^2\tan^2\theta-2(z_i-z_f)(z'-z_f)\tan^2\theta\cos\varphi}}\,dz'\,d\varphi \qquad (3.14)$$

The second part of Aij can be written as

$$A2_{ij} = \frac{1}{4\pi\varepsilon_0}\int_{\varphi_{j-1}}^{\varphi_j}\int_{\frac{(l-R)(j-1)}{n}+d+R}^{\frac{(l-R)j}{n}+d+R}\frac{(z'-z_f)\tan\theta/\cos\theta}{\sqrt{(z_i+z')^2+(z_i-z_f)^2\tan^2\theta+(z'-z_f)^2\tan^2\theta-2(z_i-z_f)(z'-z_f)\tan^2\theta\cos\varphi}}\,dz'\,d\varphi \qquad (3.15)$$

where $z_i = d + R + ctg\theta\left(\sqrt{x_i^2+y_i^2}-R\right), (x_i, y_i, z_i) \in S_i^t$.

We then can find the explicit expression of [A], whose ijth element is

$$A_{ij} = A1_{ij} - A2_{ij} \qquad (3.16)$$

We can determine matrix [B] from **Equation (3.5)**

$$\mathrm{B}_{ii} = \int_{S_i^t}\frac{1}{2\varepsilon_0}\hat{\mathrm{n}}\cdot\hat{\mathrm{z}}\mathrm{ds}$$

where $\hat{\mathrm{z}}\mathrm{ds} = (z'-d)\tan^2\theta\mathrm{dz}'\,\mathrm{d}\varphi$.

So B_{ii} can be written as

$$B_{ii} = \frac{1}{2\varepsilon_0}\int_{\varphi_{i_{m-1}}}^{\varphi_{i_m}}\int_{\frac{(l-R)i_{n-1}}{n}+d+R}^{\frac{(l-R)i_n}{n}+d+R}(z'-d)\tan^2\theta\mathrm{dz}'\,\mathrm{d}\varphi \qquad (3.17)$$

where $z_i = d + R + ctg\theta\left(\sqrt{x_i^2+y_i^2}-R\right), (x_i, y_i, z_i) \in S_i^t$, $i_n = 1,2,3,...,n$, $i_m = 1,2,3,...,m$, and $i = (i_n - 1)m + i_m$.

With [A] and [B], we can determine the continuous point spread function for the conical part of the tip from **Equation (3.9)**. $\vec{\mathrm{h}}_\mathrm{d}$ in **Equation (3.9)** is an N vector whose ith element is

$$\mathrm{h}_{\mathrm{d,i}}(\mathrm{x},\mathrm{y}) = \frac{\mathrm{z_i}}{2\pi}\left[(\mathrm{x}-\mathrm{x_i})^2 + (\mathrm{y}-\mathrm{y_i})^2 + \mathrm{z_i^2}\right]^{-\frac{3}{2}}$$

where $z_i = d + R + ctg\theta\left(\sqrt{x_i^2 + y_i^2} - R\right), (x_i, y_i, z_i) \in S_i^t$.

3.1.3 The point spread function of a tip with both spherical part and conical part

For a tip with both hemispherical part and conical part, we use the same method to segment the hemispherical part into $t_h = n_h \times m_h$ segments and the conical part into $t_c = n_c \times m_c$ segments, and form a $t \times t$ [A] matrix where $t = t_h + t_c$. As we mentioned in III, the [A] matrix represent the contribution of charge density to potential, we can thus calculated separately by dividing [A] into 4 segments: $[A_1]$ with elements $A_{ij}, i = 1,2,...,t_h, j = 1,2,...,t_h$, represents the contribution of charge dowelling on hemispherical part to its own potential, $[A_2]$ with elements $A_{ij}, i = t_{h+1}, t_{h+2},...,t, j = 1,2,...,t_h$, represents the contribution of charge dowelling on hemispherical part to the potential on conical part, $[A_3]$ with elements $A_{ij}, i = 1,2,...,t_h, j = t_{h+1}, t_{h+2},...,t$, represents the contribution of charge on conical part to hemispherical part, and $[A_4]$ with elements $A_{ij}, i = t_{h+1}, t_{h+2},...,t, j = t_{h+1}, t_{h+2},...,t$, represents the contribution of charge on conical part to itself. $[A_1]$ and $[A_4]$ were already solved in III. A and III. B. $[A_2]$ and $[A_3]$ can be calculated using the same equation for $[A_1]$ and $[A_4]$ but with different z_i, indicating the influence on the other part of the tip surface.

We choose typical KPFM tip parameters: length $l = 10\mu m$, half-aperture angle $\theta = 22.5^\circ$. One-dimensional point spread functions calculated for various tip parameters are shown in **Figure 5 (c), (d)**.

3.1.4 The point spread functions of a tip consisted of spherical part, conical part with a carbon nanotube attached

For a tip consist of hemispherical part, conical part, and a carbon nanotube attached (**Figure 4**), we use the same method to segment the spherical part into $t_h = n_h \times m_h$ segments, the conical part into $t_c = n_c \times m_c$ segments, the wire into $t_w = n_w \times m_w$ segments and form a $t \times t$ [A] matrix where $t = t_h + t_c + t_w$. The [A] matrix represents the contribution of charge density to potential, we can thus calculated separately by dividing [A] into 9 segments. Each segment represents the contribution of the charge dowelling on a segment to the potential of one of the three segments.

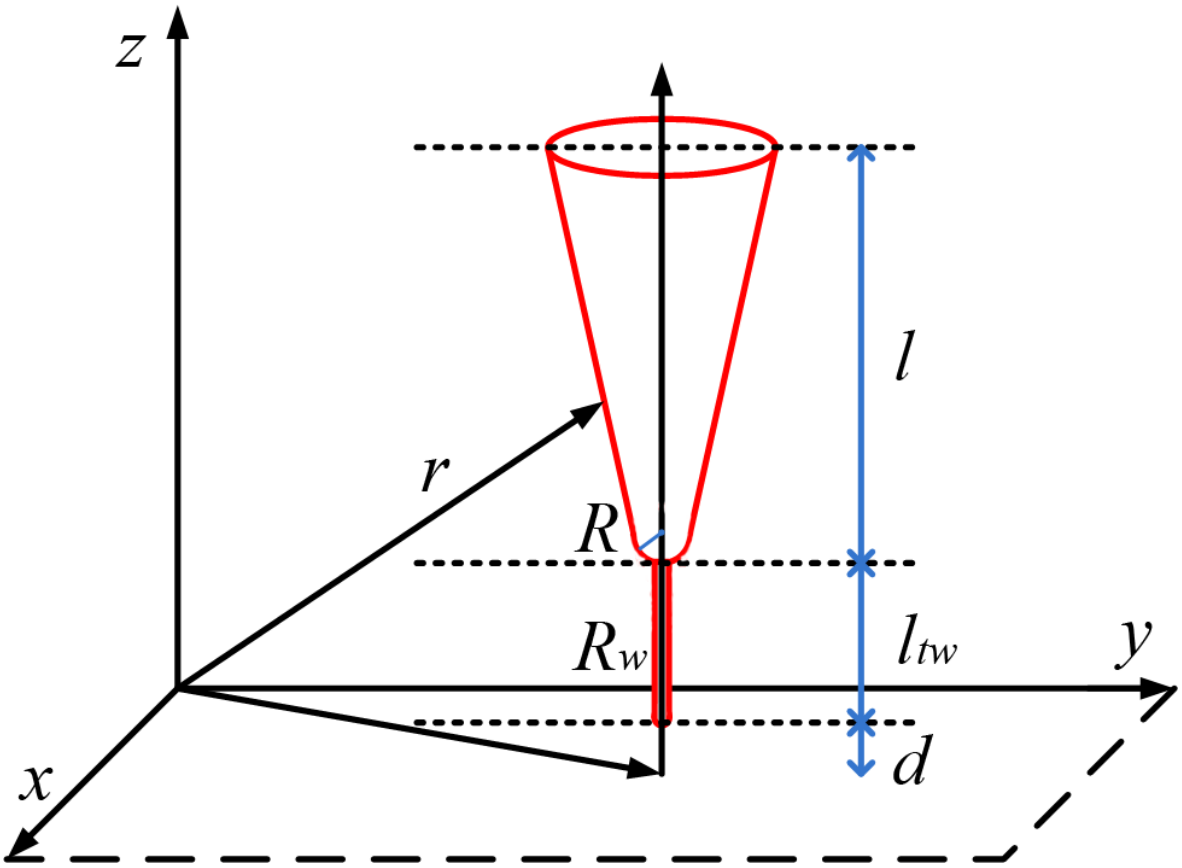

Figure 4. A tip consisted of hemispherical part, conical part with a carbon nanotube attached over flat sample surface

We choose typical KPFM tip parameters: length $l = 10\mu m$, half-aperture angle $\theta = 22.5^{\circ}$, tip radius R = 15 nm. One-dimensional point spread functions calculated for various tip parameters are shown in **Figure 7**. As we can see from **Figure 7 (a)**, the area under the curve of tip consisted of only spherical and conical part is broader than the ones of tips with carbon nanotube attached. That is due to the effect of the conical tip bodies, which will lower the resolution of KPFM measurement. Also, as the length of the carbon nanotube increases, the PSF gets sharper. Therefore, attaching a carbon nanotube can reduce the tip body effect in AM-KPFM measurements, and gives better resolution as we can see from **Figure 7**.

3.2 THE POINT SPREAD FUNCTIONS FOR DIFFERENT TIP SHAPES IN FM-KPFM MEASUREMENT

For FM-KPFM, we can utilize the same method to split the tip surface and assume each small area has the same charge density. From **Equation (3.2) and (3.3)**, we can see that $\vec{\sigma}$ is a function of both V and d.

Here minimum force gradient condition **Equation (2.18)** is utilized. We need to plug **Equation (3.3)** into minimum force gradient condition to solve for V. We can use the same [A] and [B] matrix in **Section 3.1**. The minimum force gradient condition $\frac{\partial^2 \mathrm{F_z}}{\partial \mathrm{d} \partial \mathrm{V}} = 0$ can be expressed via **Equation (3.4)**

$$\left(\frac{\partial^2 \vec{\sigma}}{\partial d \partial V}\right)^t [B]\vec{\sigma} + \left(\frac{\partial \vec{\sigma}}{\partial d}\right)^t [B]\frac{\partial \vec{\sigma}}{\partial V} = 0 \qquad (3.18)$$

We plug **Equation (3.3)** into **Equation (3.18)** and obtain the relation between the measured tip potential and the potential produced by the dipole layer:

$$\frac{\partial\vec{\sigma}}{\partial d} = -[A]^{-1}\left\{\frac{\partial[A]}{\partial d}[A]^{-1}\left(V\vec{1} - \vec{\Phi}^{\mathrm{d}}\right) + \frac{\partial\vec{\Phi}^{\mathrm{d}}}{\partial d}\right\} \qquad (3.19)$$

$$\frac{\partial^2\vec{\sigma}}{\partial d\partial V} = -[A]^{-1}\frac{\partial[A]}{\partial d}[A]^{-1}\vec{1} \qquad (3.20)$$

$$\mathrm{V(r)} = \frac{[P_{\Phi^d}]\vec{\Phi}^{\mathrm{d}}(\mathrm{r}) - [P_{\Phi_d^d}]\dfrac{\partial\vec{\Phi}^{\mathrm{d}}(\mathrm{r})}{\partial \mathrm{d}}}{P_V} \qquad (3.21)$$

where prefactor for V(r) is $P_V = 2\left([A]^{-1}\frac{\partial[A]}{\partial d}[A]^{-1}\vec{1}\right)^{\mathrm{t}}[\mathrm{B}][\mathrm{A}]^{-1}\vec{1}$, prefactor matrix for $\vec{\Phi}^{\mathrm{d}}(\mathrm{r})$ is $[P_{\Phi^d}] = \left([\mathrm{B}][\mathrm{A}]^{-1}\vec{1}\right)^{\mathrm{t}}[A]^{-1}\frac{\partial[A]}{\partial d}[A]^{-1} + \left([A]^{-1}\frac{\partial[A]}{\partial d}[A]^{-1}\vec{1}\right)^{\mathrm{t}}[\mathrm{B}][\mathrm{A}]^{-1}$, prefactor matrix for $\frac{\partial\vec{\Phi}^{\mathrm{d}}}{\partial d}$ is $[P_{\Phi_d^d}] = \left([\mathrm{B}][\mathrm{A}]^{-1}\vec{1}\right)^{\mathrm{t}}[A]^{-1}$.

Using (24), we find that the measured tip potential can be expressed as

$$\mathrm{V(x,y)} = \mathrm{h_{FM}(x,y)} * \Phi^{\mathrm{S}}(\mathrm{x,y}) \qquad (3.22)$$

with the continuous point spread function,

$$\mathrm{h_{FM}(x,y)} = \frac{[P_{\Phi^d}]\vec{\mathrm{h}}_{\mathrm{d}} - [P_{\Phi_d^d}]\dfrac{\partial\vec{\mathrm{h}}_{\mathrm{d}}}{\partial \mathrm{d}}}{P_V} \qquad (3.23)$$

We choose typical KPFM tip parameters: length $l = 10\mu m$, half-aperture angle $\theta = 22.5^{\circ}$,. One-dimensional point spread functions calculated for various tip shapes and parameters are shown in **Figure 6 (a), (b), (c), (d)**. In AM-KPFM, significant PSFs' differences are observed between those plots of the tips with and without conical tip body part. FM-KPFM measurement significantly eliminates the tip body effect by reducing those differences. We can see that the

area under the curves in FM-KPFM is narrower than the area in AM-KPFM. This will give FM-KPFM measurements better resolution. In order to acquire better resolution for both AM-KPFM and FM-KPFM, it is better to use the tips with carbon nanotube attached.

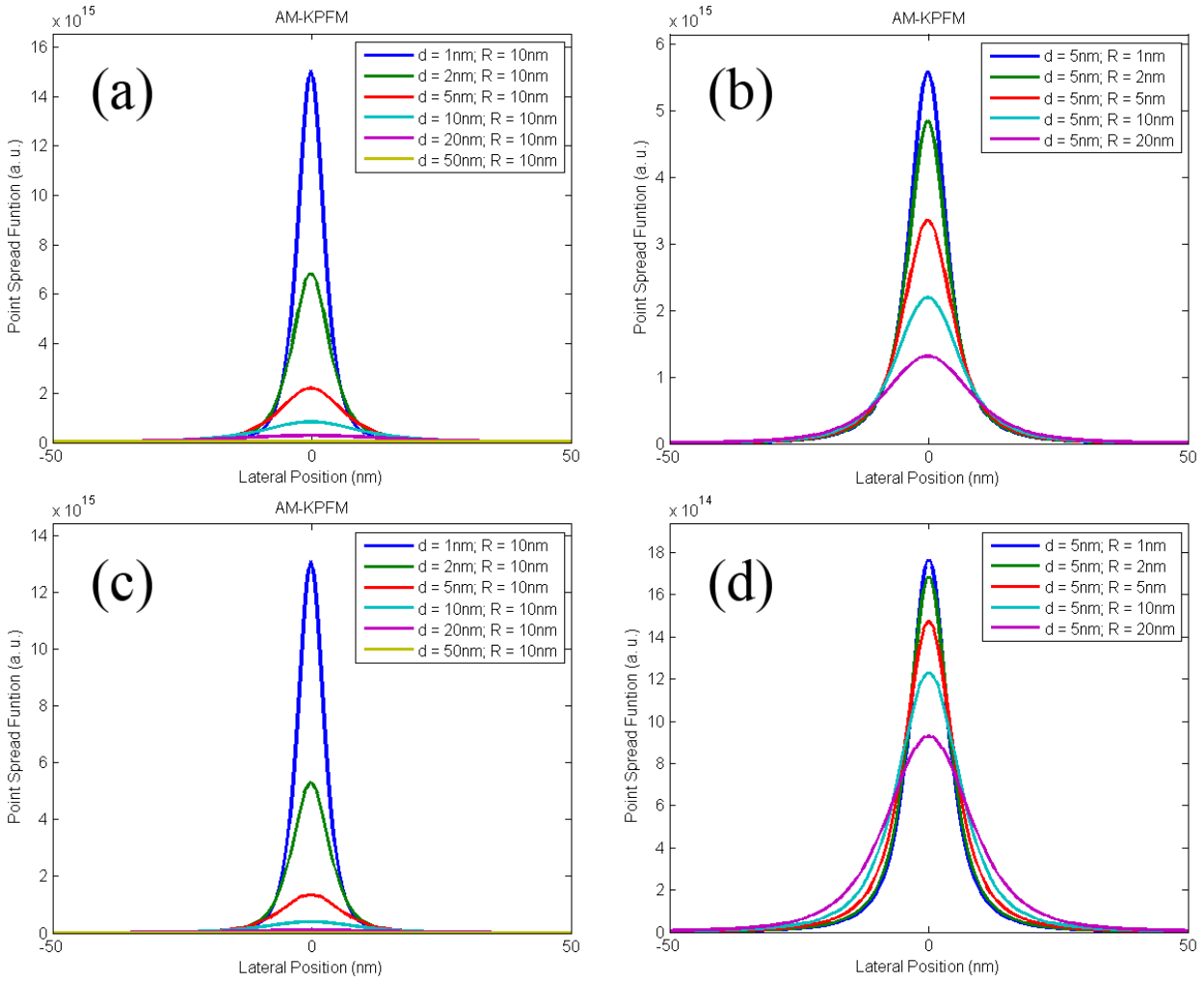

Figure 5. One-dimensional point spread functions of various tip shapes for different tip parameters in AM-KPFM measurement (a) One-dimensional PSFs of spherical tip for tip-sample distance, d of 1, 2, 5, 10, 20, 50 nm, R= 10 nm. (b) One-dimensional PSFs of spherical tip for tip apex radius, R of 1, 2, 5, 10, 20 nm, d=5 nm. (c) One-dimensional PSFs of tip consisted of spherical and conical parts for tip-sample distance, d of 1, 2, 5, 10, 20, 50 nm, R= 10 nm. (d) One-dimensional PSFs of tip consisted of spherical and conical parts for tip apex radius, R of 1, 2, 5, 10, 20 nm, d=5 nm.

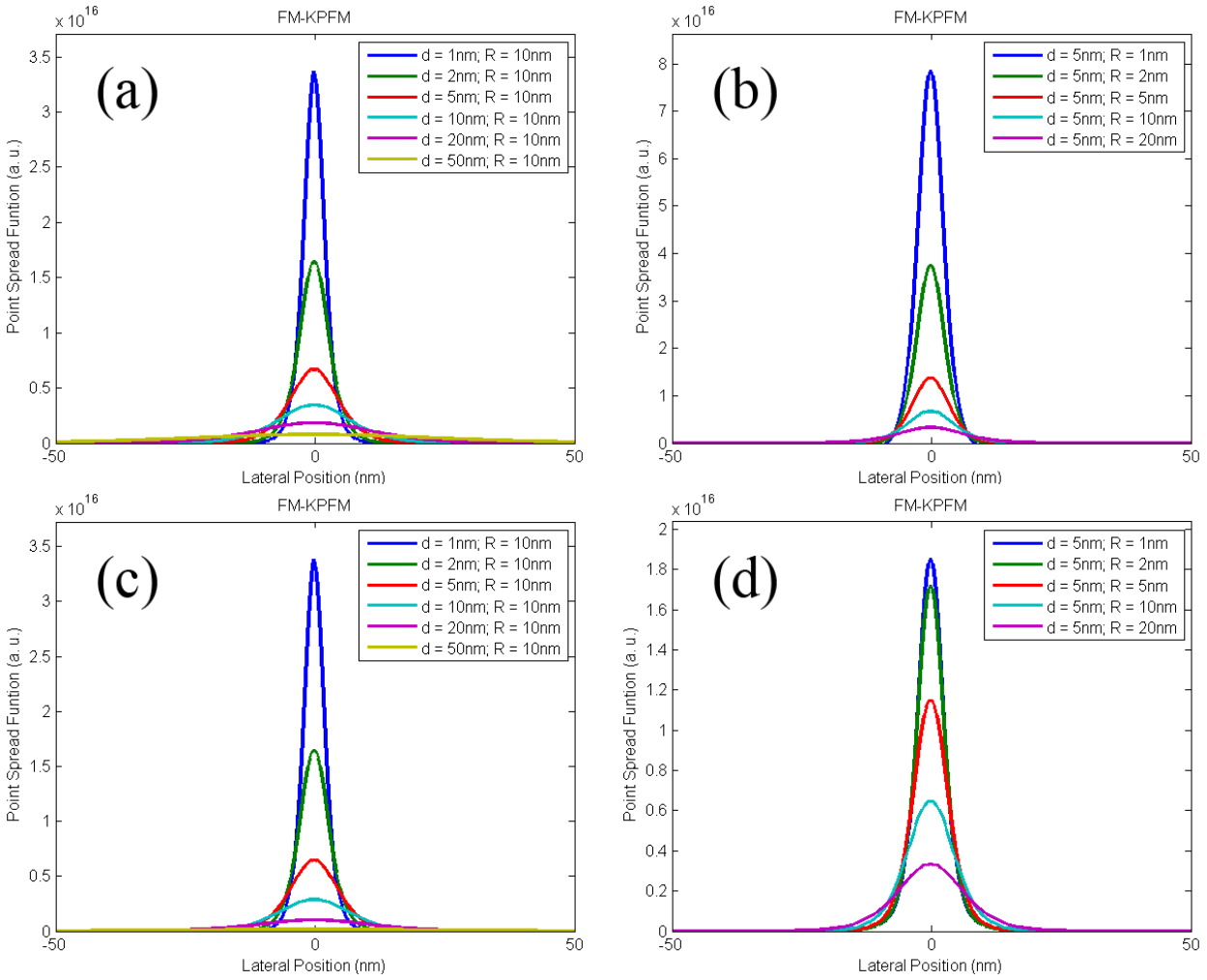

Figure 6. One-dimensional point spread functions of various tip shapes for different tip parameters in FM-KPFM measurement (a) One-dimensional PSFs of spherical tip for tip-sample distance, d of 1, 2, 5, 10, 20, 50 nm, R= 10 nm. (b) One-dimensional PSFs of spherical tip for tip apex radius, R of 1, 2, 5, 10, 20 nm, d=5 nm. (c) One-dimensional PSFs of tip consisted of spherical and conical parts for tip-sample distance, d of 1, 2, 5, 10, 20, 50 nm, R= 10 nm. (d) One-dimensional PSFs of tip consisted of spherical and conical parts for tip apex radius, R of 1, 2, 5, 10, 20 nm, d=5 nm.

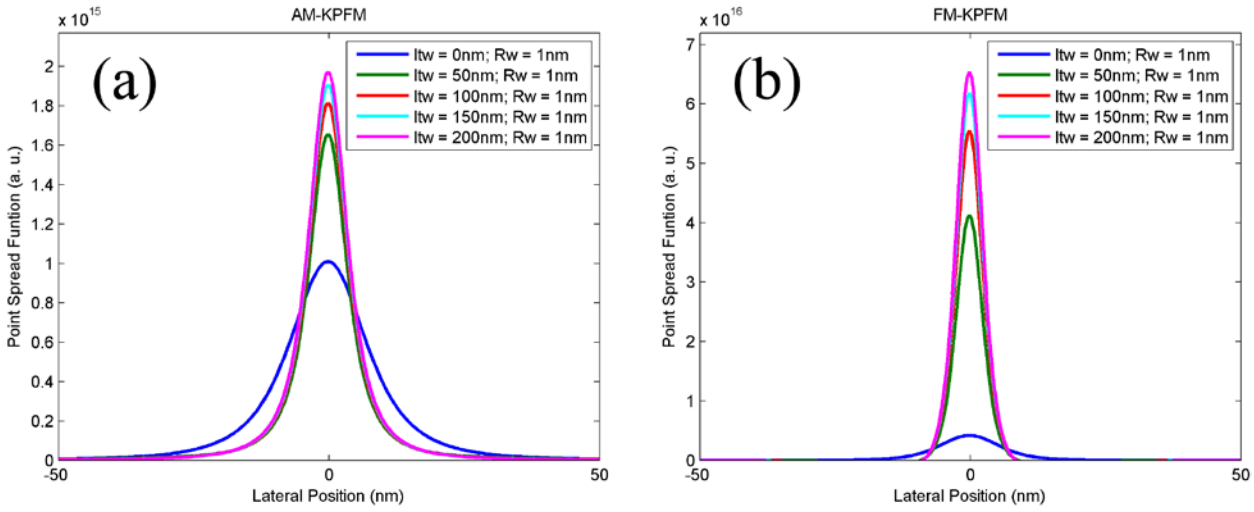

Figure 7. One-dimensional point spread functions of tip consisted of spherical part, and conical part with a carbon nanotube attached for different tip parameters (a) One-dimensional PSFs in AM-KPFM for the length of the carbon nanotube, l_{tw} of 0, 50, 100, 150, 200 nm, d = 5 nm, R= 15 nm, R_w = 1 nm. (b) One-dimensional PSFs in FM-KPFM for the length of the carbon nanotube, l_{tw} of 0, 50, 100, 150, 200 nm, d = 5 nm, R= 15 nm, R_w = 1 nm.

4.0 RESOLUTION

The resolution of KPFM has already been discussed by several authors [18, 19]. However, there is lack of a clear definition of the resolution for KPFM. Colchero et al defined the resolution for electrostatic force microscopy as the radius of a circle under the tip that contributes half to the total interaction [23]. This definition is difficult to use for analysis since the interaction is difficult to determine analytically.

We argue that the point spread function is a major determinant of the KPFM resolution. We define the resolution of KPFM using Rayleigh criterion with PSFs that have no zero in the neighborhood of their central maxima. Composite distribution can be generated using a certain PSF to convolute two points on the sample. This composite distribution has a dip in the center and two maxima. The resolution limit is defined as the distance for which the ratio of the value at the central dip in the composite intensity distribution to that at the maxima on either side is equal to 0.81 [24]. With this definition, we can analyze and compare the resolution of KPFM for different scanning parameters under different scan modes.

4.1 RESOLUTION OF KPFM WITH AMPLITUDE MODULATION

PSFs for different tip shapes are calculated to compare their effect on Rayleigh criterion resolution. We use typical KPFM tip parameters: length $l = 10\mu m$, half-aperture angle $\theta = 22.5^{\circ}$. The resolution for different tip parameters is listed in **Table 1**.

Table 1. Comparison of resolution for the tip with spherical and conical part in AM-KPFM

Rayleigh Criteria Resolution (nm)		Tip Apex Radius (nm)				
		1	2	5	10	20
Tip-Sample Distance (nm)	1	2.6	3.3	4.9	6.8	9.3
	2	4.4	5.2	7.2	9.8	13.6
	5	9.7	10.3	12.5	16.3	22.2
	10	18.8	19.5	21.1	25.0	32.0
	20	38.3	39.8	40.9	42.2	48.4
	50	110.4	109.0	105.0	101.6	101.9
	100	224.6	222.7	216.8	210.0	203.1

It shows that smaller tip-sample distance and tip apex radius gives better resolution. Comparing to tip apex radius, tip-sample distance has larger effect on the resolution. It can be seen from **Figure 8 (a)** that as tip-sample distance increasing for 1 nm to 20 nm, the effect of tip apex radius on the resolution is decreasing. Based on our calculation, we can acquire higher resolution KPFM image by limiting the value of tip-sample distance. Single-pass scan KPFM is able to control tip-sample distance to a smaller value than dual-pass scan lift-up approach, which inevitably ends up with larger tip-sample distance.

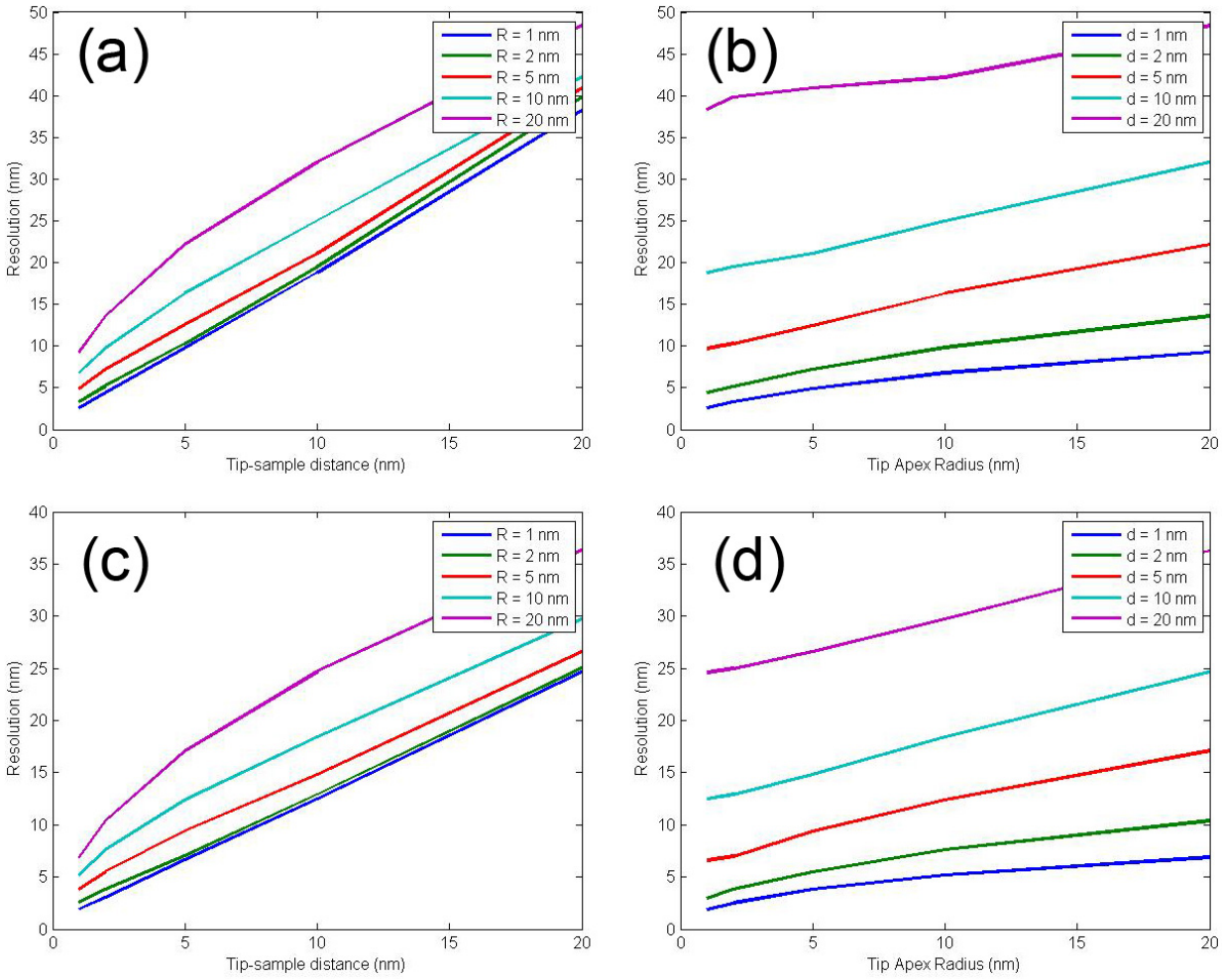

Figure 8. Resolution of AM-KPFM and FM-KPFM for different tip parameters (a) AM-KPFM Resolution vs. Tip-sample distance for tip apex radius, R=1 nm, 2 nm, 5 nm, 10 nm, 20 nm. (b) AM-KPFM Resolution vs. Tip apex radius for tip-sample distance, d=1 nm, 2 nm, 5 nm, 10 nm, 20 nm. (c) FM-KPFM Resolution vs. Tip-sample distance for tip apex radius, R=1 nm, 2 nm, 5 nm, 10 nm, 20 nm. (d) FM-KPFM Resolution vs. Tip apex radius for tip-sample distance, d=1 nm, 2 nm, 5 nm, 10 nm, 20 nm.

Finally, to further increase the resolution, we look into the effect of the tip with carbon nanotube attached, or more specifically, the carbon nanotube's effect on KPFM resolution (**Table 2**). We can see from **Table 2** that the tip with carbon nanotube attached does improve the resolution over the tip with spherical and conical part by further reducing the tip body effect. However, if we further increase the length of the carbon nanotube attached, the resolution only

has small changes. As the tip-sample distance increases, this change becomes larger but not yet substantial. Besides that, in KPFM measurements, increasing the length of the carbon nanotube may introduce other problems, such as making the carbon nanotube more fragile and easy to break.

Table 2. Comparison of resolution for the tip with carbon nanotube attached in AM-KPFM

Rayleigh Criteria Resolution (nm)		Length of the carbon nanotube (nm)				
		0*	50	100	150	200
Tip-Sample Distance (nm)	1	6.6	2.3	2.3	2.3	2.3
	2	10.5	3.9	3.9	3.9	3.9
	5	18.0	9.0	9.0	9.0	9.0
	10	27.3	17.2	16.8	16.8	16.8
	20	43.8	34.0	33.6	33.2	33.2
	50	101.4	100.78	93.8	85.0	83.8

*: Here 0 means a tip with tip radius, R = 15 nm, and no carbon nanotube attached

4.2 RESOLUTION OF KPFM WITH FREQUENCY MODULATION

Since the FM-KPFM nullifies the oscillation amplitude at $\omega_0 + \omega_e$, which is related to the force gradient, we calculated the PSF by utilizing minimum force gradient condition. The PSFs for FM-KPFM is expected to provide us better resolution. The resolution results we computed is listed in **Table 3**. It shows that FM-KPFM further increase the resolution than single scanned AM-KPFM. It can be seen from **Table 3** that as tip-sample distance increasing from 1 nm to 20 nm, the improvement of resolution over AM-KPFM measurements becomes more significant.

Zerweck et al. state that the force gradient is much more confined to the tip front end than the force [18]. Compared **Figure 8 (a) with (c), (b) with (d)**, our results support Zerweck's statement since the effect of tip apex's parameters on the resolution is larger than the one in AM-KPFM measurement.

Table 3. Comparison of resolution for the tip consisted of spherical and conical parts in FM-KPFM

Rayleigh Criteria Resolution (nm)		Tip Apex Radius (nm)				
		1	2	5	10	20
Tip-Sample Distance (nm)	1	1.9	2.5	3.8	5.2	6.9
	2	3.0	3.8	5.5	7.6	10.4
	5	6.6	7.0	9.4	12.4	17.1
	10	12.5	12.9	14.8	18.4	24.7
	20	24.6	25.0	26.6	29.7	36.3
	50	64.0	63.3	62.0	62.0	66.0
	100	130.0	128.9	126.0	124.0	124.0

We can see from **Table 4** that FM-KPFM provides better resolution for tip with carbon nanotube attached than AM-KPFM. Using a carbon nanotube attached tip with radius about 1 nm will provide a resolution of 6 nm for FM-KPFM in ambient condition when the tip-sample distance is controlled within 5nm.

Table 4. Comparison of resolution for FM-KPFM

Rayleigh Criteria Resolution (nm)		Length of the carbon nanotube (nm)				
		0*	50	100	150	200
Tip-Sample Distance (nm)	1	5.5	2.0	2.0	2.0	2.0
	2	8.2	3.1	3.1	3.1	3.1
	5	14.1	6.3	6.3	6.3	6.3
	10	21.1	11.7	11.7	11.7	11.7
	20	32.8	23.4	23.0	23.0	23.0
	50	68.0	60.4	58.0	57.4	56.8

*: Here 0 means a tip with tip radius, R = 15 nm, and no carbon nanotube attached

5.0 SENSITIVITY

In KPFM measurements, the comparison between the electrostatically induced oscillation amplitude and the noise N gives the sensitivity of the smallest measurable contact potential difference. This noise, N, consists of two major parts: the thermally induced noise of the cantilever by Brownian motion, and the noise of optical beam deflection sensor.

For the optical beam deflection sensor noise, the noise density n_{zO} is about 100 to 1000 $fm/\sqrt{Hz}$.

For the thermally induced noise, the noise density n_{zB} can be determined by:

$$n_{zB} = \sqrt{\frac{4k_bT}{Qk\omega_0}} \sqrt{\frac{1}{(1-\frac{\omega^2}{\omega_0^2})^2 + \frac{1}{Q^2}\frac{\omega^2}{\omega_0^2}}} = \sqrt{\frac{2k_bT}{Q\pi kf_0}} \sqrt{\frac{1}{(1-\frac{f^2}{f_0^2})^2 + \frac{1}{Q^2}\frac{f^2}{f_0^2}}} \quad (5.1)$$

where k_b is the Boltzmann constant, T is the absolute temperature, k is the spring constant of the cantilever, Q is the quality factor of the cantilever, ω_0 is the resonant angular frequency of the cantilever.

We also need to calculate the detected electrostatic force at the frequency of electrical drive and the oscillation amplitude at the same frequency caused by it. **Equation (1.2)** provides us an approach to determine $F_{el}(\omega_e)$ by computing $\frac{\partial C}{\partial d}$ first.

It is suspect that the carbon nanotube attached tip may not provide sufficient sensitivity because of the small area between the carbon nanotube end the sample surface. In this section, we will analyze the sensitivity of KPFM especially when a carbon nanotube attached tip is used.

5.1 ELECTROSTATIC FORCE FOR TIP WITH CARBON NANOTUBE ATTACHED

The tip and sample system can also be modeled as **Figure 4**. Besides **Equation (1.2)**, the electrostatic force between the tip and sample can be also represented by the following equation:

$$F_{el} = \int_S \frac{\varepsilon_0 E(x,y,z)^2}{2} ds = \frac{1}{2}\frac{\partial C}{\partial d} V^2 \approx \frac{\varepsilon_0 V^2}{2} \int_S \frac{1}{a(x,y,z)^2} ds \qquad (5.2)$$

where $a(x,y,z)$ is the arc length of the circular segment coming from the tip at position x, y, z.

From **Equation (5.2)**, we can get the relation

$$\frac{\partial C}{\partial d} \approx \varepsilon_0 \int_S \frac{1}{a(x,y,z)^2} ds \qquad (5.3)$$

The total electrostatic force consists three parts: spherical contribution, conical contribution, and carbon nanotube's contribution. We can evaluate these three parts separately. Typical tip parameters are used: tip radius, R=15 nm, half apex angle, $\theta = 22.5^\circ$, radius of carbon nanotube, $R_w = 1nm$.

5.1.1 Spherical contribution

For this spherical part, we can use **Figure 3** to illustrate the relation of the tip surface and the sample. Here $a(x, y, z)$ can be evaluated by the following equation

$$a(x, y, z) = \frac{\beta\left[d + l_{tw} + R\left(1 - \cos\beta\right)\right]}{\sin\beta} \quad (5.4)$$

where d is the tip-sample distance, l_{tw} is the length of the carbon nanotube.

On this spherical surface, we can construct an infinitesimal surface $\mathrm{ds} = \mathrm{R}^2 \sin\beta d\beta \mathrm{d}\varphi$. Plugging **Equation (5.4)** to **Equation (5.3)**, the derivative of the capacitance for this part $\frac{\partial C_s}{\partial d}$ can be written as

$$\frac{\partial C_s}{\partial d} = 2\pi\varepsilon_0 R^2 \int_{a\sin(R_w/R)}^{\pi/2-\theta} \frac{\sin^3\beta}{\beta^2\left[d + l_{tw} + R\left(1 - \cos\beta\right)\right]^2} d\beta \quad (5.5)$$

When $R >> R_w$ R, the analytical solution can be found by determining the upper and lower limit for **Equation (5.5)**,

$$\frac{\partial C_s}{\partial d} = 2\pi\varepsilon_0 R^2 \frac{1 - \sin\theta}{(d + l_{tw})\left[d + l_{tw} + R(1 - \sin\theta)\right]} \quad (5.6)$$

5.1.2 Conical contribution

Now we need to calculate the conical part's contribution. At height z, $a(x, y, z)$ can be evaluated by the following equation

$$a(x, y, z) = \left(\frac{\pi}{2} - \theta\right)\frac{z}{\cos\theta} \quad (5.7)$$

On this spherical surface, we can construct an infinitesimal surface $ds = (z - z_f)tan^2\theta d\varphi dz$, where $z_f = d + l_{tw} + R - R/\sin\theta$ is the apex of the cone.

Plugging **Equation (5.7)** into **Equation (5.3)**, we have

$$\frac{\partial C_c}{\partial d} = \frac{2\pi\varepsilon_0 \sin^2\theta}{(\pi/2-\theta)^2}\int_{d+l_{tw}+R(1-\sin\theta)}^{d+l_{tw}+l}\frac{z-z_f}{z^2}dz$$
$$= \frac{2\pi\varepsilon_0 \sin^2\theta}{(\pi/2-\theta)^2}\left(\ln\frac{d+l_{tw}+l}{d+l_{tw}+R(1-\sin\theta)} - 1 + \frac{R^2\cos^2\theta/\sin^2\theta}{d+l_{tw}+R(1-\sin\theta)}\right) \quad (5.8)$$

5.1.3 Carbon nanotube contribution

The front top of the carbon nanotube is modeled as a hemisphere with radius, $R_w = 1nm$. In **Figure 4**, we can see that in our model, the carbon nanotube is perpendicular to the sample surface. Since the area on the cylinder will not contribute to $\frac{\partial C}{\partial d}$, we can only consider the hemispherical part of the carbon nanotube.

We can use similar analysis as we did in **Section 5.1.2**. $\frac{\partial C_w}{\partial d}$ can be calculated by the following equation

$$\frac{\partial C_w}{\partial d} = 2\pi\varepsilon_0 \frac{R_w^2}{d(d+R_w)} \quad (5.9)$$

For a tip consisted of spherical and conical parts with a carbon nanotube attached, the derivative of capacitance C is given by:

$$\frac{\partial C}{\partial d} = 2\pi\varepsilon_0\left[\frac{R^2(1-\sin\theta)}{(d+l_{tw})[d+l_{tw}+R(1-\sin\theta)]} + \frac{R_w^2}{d(d+R_w)} + \frac{\sin^2\theta}{(\pi/2-\theta)^2}\left(\ln\frac{d+l_{tw}+l}{d+l_{tw}+R(1-\sin\theta)} - 1 + \frac{R^2\cos^2\theta/\sin^2\theta}{d+l_{tw}+R(1-\sin\theta)}\right)\right] \quad (5.10)$$

5.2 SENSITIVITY OF AM-KPFM

In AM-KPFM, the electrostatically induced amplitude at lock-in frequency can be estimated by modeling the cantilever as a harmonic oscillator with resonant angular frequency ω_0, quality factor Q, and spring constant k. The oscillation amplitude A at drive frequency ω under a driving force, $F_d \cos(\omega t)$, is given by the following equation:

$$A = \frac{F_d}{k} \sqrt{\frac{1}{(1-\frac{\omega^2}{\omega_0^2})^2 + \frac{1}{Q^2}\frac{\omega^2}{\omega_0^2}}} \quad (5.11)$$

According to **Equation (1.2)**, $F_d = \partial C/\partial d \left(V_{dc} - V_{global}\right) V_{ac}$, the oscillation amplitude at ω becomes:

$$A_e = \frac{\partial C/\partial d \left(V_{dc} - V_{global}\right) V_{ac}}{k} \sqrt{\frac{1}{(1-\frac{\omega^2}{\omega_0^2})^2 + \frac{1}{Q^2}\frac{\omega^2}{\omega_0^2}}} \quad (5.12)$$

For a tip consisted of spherical and conical parts with a carbon nanotube attached, the derivative of capacitance C is given by **Equation (5.10)**

By letting $A_e = n_{zO}\sqrt{B}$ (B is the band response width of the lock-in amplifier), we can find the minimum detectable potential difference limited by the optical beam deflection sensor noise:

$$V_{mO} = \frac{k n_{zO}\sqrt{B}}{\partial C/\partial d\, V_{ac}} \sqrt{(1-\frac{\omega^2}{\omega_0^2})^2 + \frac{1}{Q^2}\frac{\omega^2}{\omega_0^2}} \quad (5.13)$$

Letting $A_e = n_{zB}\sqrt{B}$, we can find the minimum detectable potential difference limited by the thermally induced noise:

$$V_{mB} = \sqrt{\frac{4k_b TkB}{Q\omega_0}} \frac{1}{\partial C/\partial d\, V_{ac}} \quad (5.14)$$

The combination of the sensitivity derived from the two noise sources become the ultimate sensitivity, which can be determined as:

$$V_{CPD,\min} = \sqrt{V_{mO}^2 + V_{mB}^2} \quad (5.15)$$

For a probe (Bruker-AXS SCM-PIT, coated with Pt/Ir) with k=2.8N/m, f_0 =75kHz, Q=100 in ambient condition, $\theta = 22.5^\circ$ and the following typical parameters: T=300K, B=5Hz, $V_{ac} = 2V$, the sensitivities corresponding to tip-surface distance and the length of the carbon nanotube are plotted in **Figure 9 (a), (b)** for single pass AM-KPFM. For dual-pass lift-up scan AM-KPFM, the sensitivities are plotted in **Figure 9 (c), (d)** for comparison.

5.3 SENSITIVITY OF FM-KPFM

In FM-KPFM measurements, with the presence of small force gradient $\partial F/\partial d$, the phase of the oscillation at the drive frequency ω_0 shifts $\Delta\varphi = -Q(\partial F/\partial d)/k$. Noting **Equation (1)**, the oscillation of cantilever at resonant frequency becomes

$$A(t) = A_0 \sin\left\{\omega_m t - \frac{Q}{2k}\frac{\partial^2 C}{\partial d^2}\left[\left(\left(V_{dc} - V_{global}\right)^2 + \frac{1}{2}V_{ac}^2\right) + 2\left(V_{dc} - V_{global}\right)V_{ac}\cos(\omega_e t) - \frac{1}{2}V_{ac}^2\cos(2\omega_e t)\right]\right\} \quad (5.16)$$

When the phase shift is small, **Equation (5.16)** can be written as the following form

$$A(t) = A_0 \sin(\omega_m t - \phi) + 2A_{m\pm e}\sin(\omega_e t)\cos(\omega_m t - \phi) + 2A_{m\pm 2e}\cos(2\omega_e t)\cos(\omega_m t - \phi) \quad (5.17)$$

where

$$\phi = \frac{Q}{2k}\frac{\partial^2 C}{\partial d^2}\left(\left(V_{dc} - V_{global}\right)^2 + \frac{1}{2}V_{ac}^2\right),$$

$$A_{m\pm e} = -A_0 \frac{Q}{2k}\frac{\partial^2 C}{\partial d^2}\left(V_{dc} - V_{global}\right)V_{ac},$$

$$A_{m\pm 2e} = -A_0 \frac{Q}{8k}\frac{\partial^2 C}{\partial d^2}V_{ac}^2$$

This $A_{m\pm e}$ represents the oscillation amplitude at the sidebands $\omega_m \pm \omega_e$. The mechanical oscillation A_0 is fairly close to the tip-sample distance d in single pass KPFM. The deflection sensor noise and the thermally induced noise can be calculated using the similar way as we explained in **Section 5.2**.

By letting $A_e = n_{zO}\sqrt{B}$ (B is the band response width of the lock-in amplifier), we can find the minimum detectable potential difference limited by the optical beam deflection sensor noise:

$$V_{mO} = \frac{-2kn_{zO}\sqrt{B}}{A_0 Q\,\partial^2 C/\partial d^2 V_{ac}} \quad (5.18)$$

Letting $A_e = n_{zB}\sqrt{B}$, we can find the minimum detectable potential difference limited by the thermally induced noise:

$$V_{mB} = -\sqrt{\frac{16k_b TkB}{Q^3\omega_0}}\sqrt{\frac{1}{(1-\frac{\omega^2}{\omega_0^2})^2 + \frac{1}{Q^2}\frac{\omega^2}{\omega_0^2}}}\frac{1}{\partial^2 C/\partial d^2 V_{ac}} \quad (5.19)$$

The combination of the sensitivity derived from the two noise sources become the ultimate sensitivity, which can be determined as:

$$V_{CPD,\min} = \sqrt{V_{mO}^2 + V_{mB}^2} \quad (5.20)$$

For a probe (Bruker-AXS SCM-PIT, coated with Pt/Ir) with k=2.8N/m, f_0 =75kHz, Q=100 in ambient condition, $\theta = 22.5^{\circ}$ and the following typical parameters: T=300K, B=5Hz, $V_{ac} = 2V$, the sensitivities corresponding to tip-surface distance and the length of the carbon nanotube are plotted in **Figure 10 (a), (b)** for FM-KPFM.

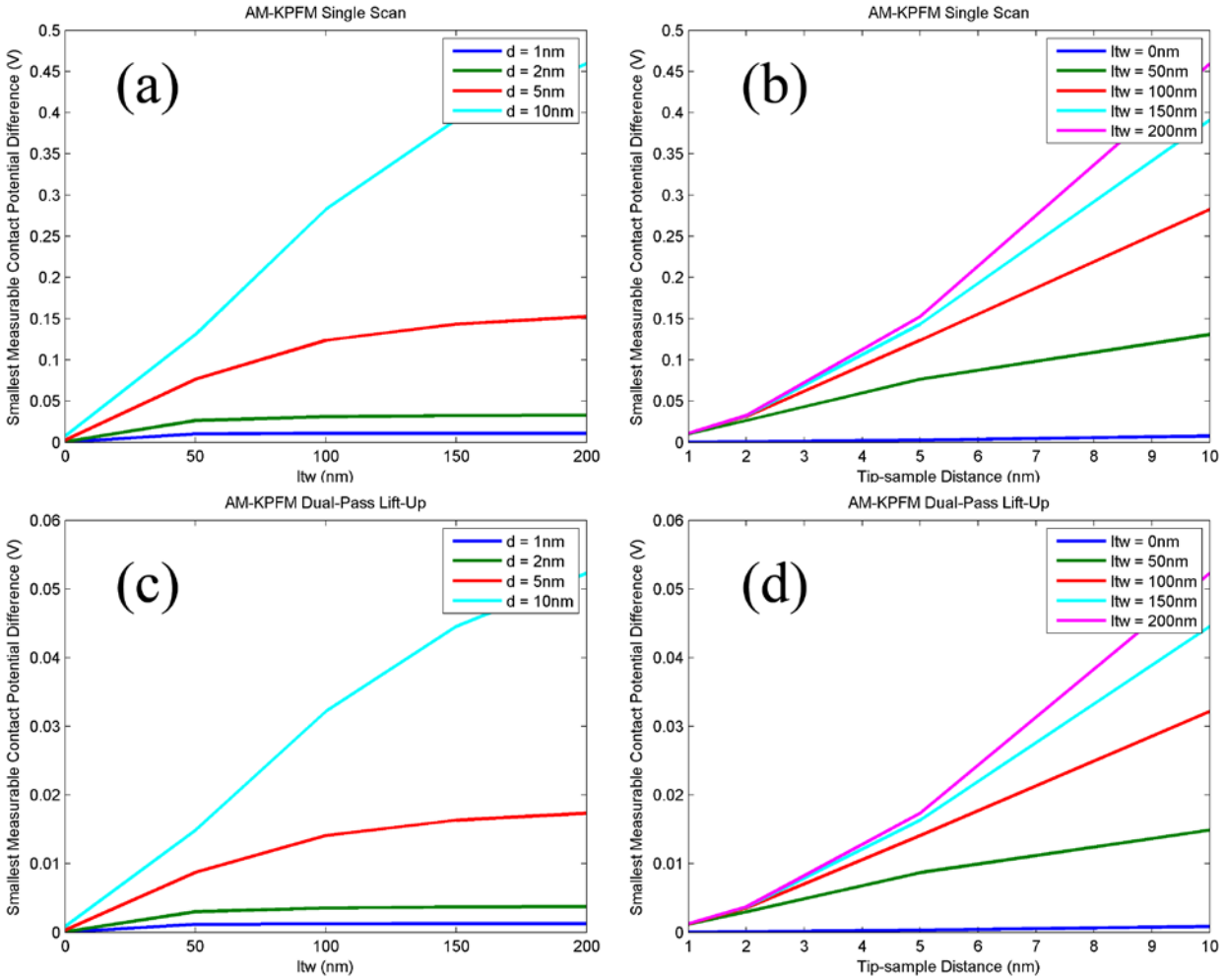

Figure 9. Sensitivity of tips with carbon nanotube attached in AM-KPFM, l_{tw} of 0, 50, 100, 150, 200 nm, d=1, 2, 5, 10 nm, R=15 nm, R_w =1nm (a) Sensitivity of AM-KPFM single scan vs. l_{tw} with different tip-sample distances, d. (b) Sensitivity of AM-KPFM single scan vs. tip-sample distances d with different l_{tw}. (c) Sensitivity of AM-KPFM

dual-pass lift-up scan vs. l_{tw} with different tip-sample distances, d. (d) Sensitivity of AM-KPFM dual-pass lift-up scan vs. tip-sample distances d with different l_{tw}.

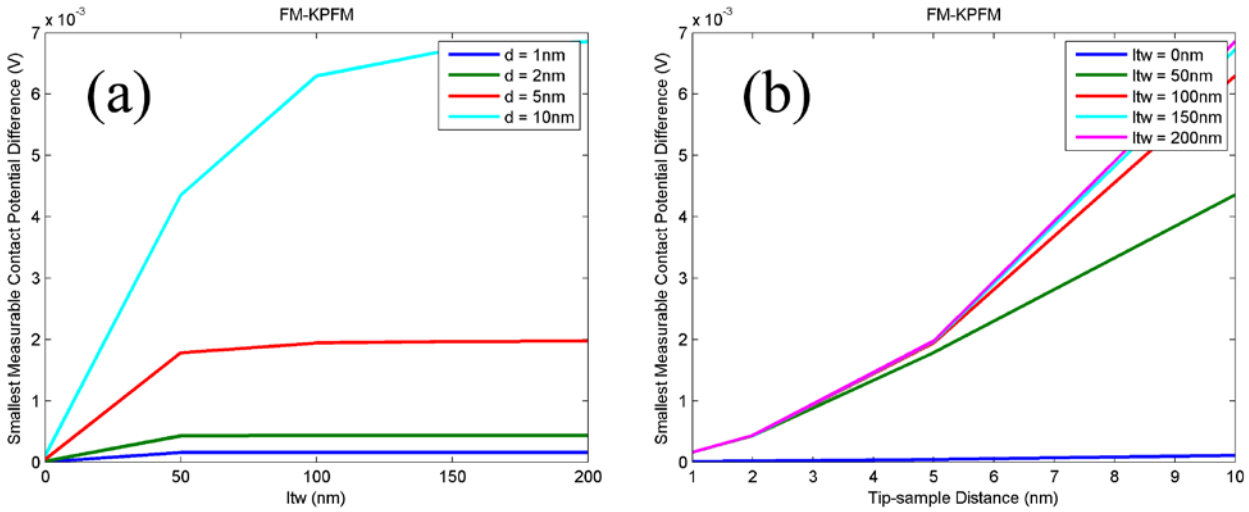

Figure 10.Sensitivity of tips with carbon nanotube attached in FM-KPFM, l_{tw} of 0, 50, 100, 150, 200 nm, d=1, 2, 5, 10 nm, R=15 nm, R_w=1nm (a) Sensitivity vs. l_{tw} with different tip-sample distances, d. (b) Sensitivity vs. tip-sample distances d with different l_{tw}.

5.4 SENSITIVITY COMPARASION

According to **Equation 5.13 and 5.14**, it can be easily seen that the minimum detectable voltage is proportional to tip-sample distance, d (**Figure 9 (b), (d)**) and inverse proportional to the tip radius R. Thus, smaller tip-sample distance results in both better sensitivity and resolution (See **Section 4**). However, a better sensitivity requires a larger tip apex radius, which leads to lower resolution.

The sensitivity in single-pass scan is given in **Figure 9 (a), (b)**. Dual-pass lift-up scan mode results is plotted in **Figure 9 (c), (d)**. Even though the sensitivity of single-pass scan AM-

KPFM is lower than that of dual-pass scan AM-KPFM for same tip-sample distance. In practical usage, the sensitivity of single-pass scan AM-KPFM is comparable to that of dual-pass scan AM-KPFM considering it is much easier to maintain a smaller tip-sample distance in single-pass scan mode. If we consider the typical parameters we are using for these two modes without carbon nanotube attached on tip, single-pass scan mode offers similar sensitivity, $V_{CPD,\min}$ =2.8mV (tip-sample distance, d=5nm, tip radius, R=15nm), to dual-pass lift-up scan mode, $V_{CPD,\min}$ =2.6mV (d=20nm, R=15nm). When a carbon nanotube is attached, the comparison is similar. In general the sensitivity of KPFM has lower sensitivity when a carbon nanotube attached tip is used.

From the finding, it can be seen that FM-KPFM provides better sensitivity as well as better resolution than AM-KPFM. In **Figure 10**, we can see the sensitivity of FM-KPFM is at least two orders of magnitude better than single-pass AM-KPFM. If we compare the sensitivity of FM-KPFM using a carbon nanotube attached tip and that of dual-pass lift-up AM-KPFM using bare tip, FM-KPFM still outperforms dual-pass lift-up scan mode AM-KPFM under same operating conditions. .

As we can see from **Figure 9** and **Figure 10**, the sensitivity deteriorates as the length of the carbon nanotube increases when the tip-sample distance is larger. Therefore, a short length of carbon nanotube is beneficial to the sensitivity. Considering a longer carbon nanotube does not improve the resolution so much (**Table 4**), we suggest that the length of carbon nanotube should less than 50nm in order to obtain both better resolution and sensitivity.

6.0 CONCLUSION

In this thesis, we study the resolution of KPFM and understand different working mechanisms and probe parameters, we find the analytical expressions of point spread function by establishing an electrostatic model. Analytical expressions of PSFs of both amplitude-modulation and frequency-modulation Kelvin Probe Force Microscopy for tips with and without carbon nanotube attached are calculated. From these PSFs, we can find the resolution limit and sensitivity in KPFM measurement.

Our study shows that tips with carbon nanotube attached gives better resolution and relatively good sensitivity. Since the single-pass scan KPFM is able to precisely control the tip-sample distance to a much smaller value than dual-pass lift-up scan KPFM, it is safe to say that single-pass scan KPFM has the ability to achieve higher resolution than dual-pass scan KPFM. Also, FM-KPFM can achieve better resolution and sensitivity than AM-KPFM. Attaching a carbon nanotube will provide better resolution. However, further increase the length of the carbon nanotube may not get better result, and can cause other problems, such as making the carbon nanotube easier to break.

Our study also shows that the single-pass scan KPFM has comparable or even better sensitivity than dual-pass lift-up scan KPFM in AM-KPFM measurements. In FM-KPFM measurements, the sensitivity performance is much better than AM-KPFM. Attaching a carbon

nanotube to the tip will reduce the sensitivity. This is another reason why we should not use very long carbon nanotube in this circumstance.

BIBLIOGRAPHY

[1] J. D. Wei, S. F. Li, A. Atamuratov, H. H. Wehmann and A. Waag, Applied Physics Letters 97(17), 172111-172113 (2010).

[2] H. R. Moutinho, R. G. Dhere, C. S. Jiang, Y. Yan, D. S. Albin and M. M. Al-Jassim, Journal of Applied Physics 108(7), 074503-074507 (2010).

[3] K. Skorupska, C. Pettenkofer, S. Sadewasser, F. Streicher, W. Haiss and H. J. Lewerenz, physica status solidi (b) 248(2), 361-369 (2011).

[4] C. Baumgart, A.-D. Müller, F. Müller and H. Schmidt, physica status solidi (a), (2011).

[5] C. Baumgart, M. Helm and H. Schmidt, Physical Review B 80(8), 085305 (2009).

[6] M. Ligowski, D. Moraru, M. Anwar, T. Mizuno, R. Jablonski and M. Tabe, Applied Physics Letters 93(14), 142101 (2008).

[7] H. Hoppe, T. Glatzel, M. Niggemann, A. Hinsch, M.C. Lux-Steiner, N.S. Sariciftci, Nano Lett. 5 (2005) 269.

[8] T. Hallam, C.M. Duffy, T. Minakata, M. Ando, H. Sirringhaus, Nanotechnology 20 (2009) 025203.

[9] L.M. Liu, G.Y. Li, Applied Physics Letters 96 (2010) 083302.

[10] P. Zhang and H. F. Cantiello, Applied Physics Letters 95(11), 113703-113703 (2009).

[11] P. Zhang and H. F. Cantiello, Applied Physics Letters 95(3), 033701-033703 (2009).

[12] C. Leung, H. Kinns, B. W. Hoogenboom, S. Howorka and P. Mesquida, Nano Letters 9(7), 2769-2773 (2009).

[13] C.-S. Jiang, H. R. Moutinho, R. Reedy, M. M. Al-Jassim and A. Blosse, Journal of Applied Physics 104(10), 104501 (2008).

[14] H.Hoppe, T. Glatzel, M. Niggemann, A. Hinsch, M. C. Lux-Steiner and N. S. Sariciftci, Nano Letters 5(2), 269-274 (2005).

[15] M. Takihara, T. Takahashi and T. Ujihara, Applied Physics Letters 95(19), 191908 (2009).

[16] H. R. Moutinho, R. G. Dhere, C.-S. Jiang, Y. Yan, D. S. Albin and M. M. Al-Jassim, Journal of Applied Physics 108(7), 074503 (2010).

[17] M. Kaneko, A. Hinoki, A. Suzuki, T. Araki and Y. Nanishi, 2008 (unpublished).

[18] U. Zerweck, C. Loppacher, T. Otto, S. Grafstrom, and L. M. Eng, Physical Review B, Volume 71, 125424 (2005)

[19] H. O. Jacobs, P. Leuchtmann, O. J. Homan, and A. Stemmer, J. Appl.Phys. 84, 1168 (1998).

[20] E. Strassburg, A. Boag and Y. Rosenwaks, Review of Scintific Instruments 76, 083705 (2005).

[21] Jackson, Classical Electrodynamics 3rd Edition, 1998

[22] S. Hudlet, M. Saint Jean, C. Guthmann, and J. Berger, Eur. Phys. J. B 2,5 (1998).

[23] J. Colchero, A. Gil, and A. M. Baro, Physical Review B, Volume 64, 245403 (2001)

[24] A. J. den Dekker and A. van den Bos, J. Opt. Soc. Am. A 14 (3), 547-557 (1997).

[25] X. D. Ding, J. An, J. B. Xu, C. Li and R. Y. Zeng, Applied Physics Letters 94 (22), 223109-223103 (2009).

[26] Y.W. Chen, N. Miyanaga, M. Yamanaka, T. Yamanaka, S. Nakai, T. Iguchi, M. Nakazawa, T. Iida, and S. Tamura, IEEE Trans. Electronics E78-C, 1787 (1995).

[27] Z. Zhao, Y. Ding, J. Dong, Y. Hao, S. Wu, L. Cao, and Y. Pu, Plasma Phys. Controlled Fusion 49,1145 (2007).

[28] Weixin Qian, S. Qi, W. Wang, J. Cheng, and D. Liu, Review of Scientific Instruments, 82, 093504 (2011)